

XMM-Newton Archival Study of the ULX Population in Nearby Galaxies

Lisa M. Winter

Astronomy Department, University of Maryland, College Park, MD 20742

`lwinter@astro.umd.edu`

Richard F. Mushotzky

Goddard Space Flight Center, Greenbelt, MD 20771

`richard@milkyway.gsfc.nasa.gov`

Christopher S. Reynolds

Astronomy Department, University of Maryland, College Park, MD 20742

`chris@astro.umd.edu`

ABSTRACT

We have conducted an archival *XMM-Newton* study of the bright X-ray point sources in 32 nearby galaxies. From our list of approximately 100 point sources, we attempt to determine if there is a low-state counterpart to the Ultraluminous X-ray (ULX) population, testing the specific predictions of the IMBH hypothesis. Indeed, 16 sources in our sample match the criteria we set for a low-state ULX, namely, $L_X > 10^{38} \text{ erg s}^{-1}$ and a spectrum well fit with a simple absorbed power law. Further, we find evidence for 26 ULXs which are well fit by a combined blackbody and a power law, similar to high-state Galactic black holes. As in Galactic black hole systems, the spectral indices, Γ , of the low-state objects, as well as the luminosities, tend to be lower than those of the high-state objects. The observed range of blackbody temperatures is 0.1-1 keV with the most luminous systems tending toward the lowest temperatures. We also find a class of object whose properties (luminosity, blackbody temperature, and power law slopes) are very similar to those of galactic stellar mass black holes. In addition, we find a subset of these objects that can be best fit by a Comptonized spectrum similar to that used for Galactic black holes in the “very high” state, when they are radiating near the Eddington limit.

Subject headings: galaxies: general — surveys — X-rays:binaries — accretion, accretion discs

1. Introduction

Through X-ray observations of nearby galaxies, a class of Ultraluminous X-ray (ULX) sources has emerged. These are pointlike, non-nuclear sources with observed luminosities greater than $10^{39} \text{ erg s}^{-1}$ (Miller & Colbert 2004). Of most interest are those sources with bolometric luminosities in excess of the Eddington limit for a 20 M_\odot black hole, or $L_{bol} > 2.8 \times 10^{39} \text{ erg s}^{-1}$. The true nature of these sources is unclear, and this class most likely includes several different types of objects. Though some of these sources are located within a few parsecs of their host galaxy's dynamical center, they do not exhibit many of the characteristics of active galactic nuclei (AGN). Because the ratio of X-ray to optical flux is a factor of 10 greater than that of AGN (Anderson et al. 2003; Stocke et al. 1983), these objects are fairly easy to recognize in X-ray imaging data.

Assuming that the Eddington limit is obeyed by black hole accretion, the existence of such luminous non-AGN sources presents a puzzle. Several models have been proposed to account for the high luminosities of the ULXs. Among these are relativistic and non-relativistic beaming from stellar-mass black hole systems (Reynolds et al. 1997; King et al. 2001; Kording et al. 2002) and accretion of matter into intermediate mass black holes (IMBH). In several ULX systems (NGC 1313 X-2, M81 X-9, etc.), detection of emission nebulae surrounding the ULX supports isotropic emission from the central source (Pakull & Mirioni 2003), which cannot be described through beaming. Further, a number of ULX (NGC1313 X-1, etc.) X-ray spectra are best fit with combined multi-component blackbody (MCD) and power law fits, similar to Galactic black holes in their high-state. Recently, Miller, Fabian, & Miller (2004) find that many spectral fits of ULX require cool accretion disk temperatures of approximately 100 eV. The theoretical relationship between black hole mass and disk temperature ($T \propto M^{-1/4}$) has been observed to hold true for stellar mass (typically around 1 keV) and supermassive (around 10-100 eV) black holes (Makishima et al. 2000; Porquet et al. 2004; Gierliński & Done 2004). Using these scaling relations, the cool accretion disk ULXs would correspond to a population of high-state IMBHs with masses of $\approx 16 - 10^4 \text{ M}_\odot$.

If ULXs do not obey the Eddington limit, they could be the result of an outburst (such as can occur in low mass X-ray binaries within our own Galaxy). Jonker & Nelemans (2004) find evidence for approximately 5 Galactic black hole X-ray binaries which exhibit luminosities in the ULX range during outbursts. These sources would appear as transient ULXs. The typical time scale for outburst of Galactic X-ray transients is a few days to rise from quiescent level with a decline from peak brightness to quiescent value of 30 - 40 days (Chen, Schrader, & Livio 1997). Another possible explanation is super-Eddington emission from accretion disks surrounding stellar mass black holes (Begelman 2002; Ebisawa et al. 2003). Sources of this type would be expected to have soft X-ray components well modeled by hot accretion disks ($\approx 1.3 - 2.0 \text{ keV}$) similar to superluminal X-ray sources in the Galaxy (e.g. Belloni et al. 1997).

If some ULXs do indeed represent a class of high-state IMBHs, similar to the high-state stellar mass black holes in our galaxy, we might also expect to see the low-state objects from this same population. In Galactic black hole systems, the low-state is generally characterized by lower

luminosity, with $L < 0.1 L_{Edd}$ (Done & Gierlinski 2003), and a power law photon spectrum, typically with index $\Gamma \approx 1.7$ (McClintock & Remillard 2004). In this study we seek to test a direct prediction of the IMBH hypothesis; namely, whether there are sources with properties consistent with what we expect of low-state IMBHS. Our goal is to find these “low-state” sources, if they exist, classify the properties of both high-state and low-state ULXs, and test whether these data are consistent or inconsistent with the predictions of the IMBH hypothesis.

We present the results of a detailed analysis of ULXs in nearby galaxies observed with the European Space Agency’s *XMM-Newton* observatory. Only *XMM-Newton* provides the count rates and bandpass necessary to distinguish different spectral models for most ULXs and accurately determine both the temperature of the thermal component expected for high-state objects and whether this component is required in the spectral modeling of these objects.

In Section 2, we detail the observations examined from the *XMM-Newton* archives and explain the data analysis for the individual point sources. In Sections 3 and 4, we discuss the spectral fitting technique as well as simulations we conducted to determine their validity. We discuss the implications of our results in Section 5.

2. Observations and Data Reduction

The data used in this investigation were drawn from the *XMM-Newton* public data archive. Assuming that low-state ULXs exist in the luminosity range of $10^{38-39} \text{ erg s}^{-1}$, we conducted simulations to determine the optimum criteria for observations capable of resolving point sources of this luminosity. Our simulations provided a guide for choosing which of the vast number of archival XMM datasets we should examine. This luminosity range was chosen on the assumption that an approximately $100 M_{\odot}$ black hole would radiate at $\approx 10\%$ of the L_{Edd} in the low-state (Done & Gierlinski 2003).

Within the luminosity range of interest ($L_X > 10^{38} \text{ erg s}^{-1}$), there are a number of known objects that could be confused with ULX sources. One type of source is supernova remnants (SNRs). These sources are often easy to distinguish based on their characteristic spectrum: with poor signal to noise we expect a steep power law and as the signal to noise increases, emission lines become clearly visible. Super-Eddington accreting neutron stars have been observed to have luminosities within this range for a short period of time. Neutron star X-ray binaries often have spectra well fit by a hot multi-color disk blackbody model, or with low signal to noise, by a bremsstrahlung model. Both models have similar curvature and a 0.7-2.0 keV blackbody model is indistinguishable from the bremsstrahlung model. We chose to use the bremsstrahlung model because it is the simpler model and gives an adequate qualitative description to the data. We expect that for low temperature bremsstrahlung sources, the spectrum should be easily distinguishable from a power law with $\Gamma \approx 1.7$ (as is expected for a low-state object). If, however, the neutron star spectrum has $kT > 5 \text{ keV}$, as observed for some NS X-ray binaries, our simulations show we can not distinguish

between the power law and bremsstrahlung models.

The most common sources we expected to find in this luminosity range were the analogs to Galactic black hole X-ray binaries in their high-state. These sources typically have spectra well fit by a blackbody with temperature of ≈ 1.0 keV combined with a power law with index $\Gamma \approx 2.5$. Our simulations sought to determine the number of photons required to distinguish between spectral fits corresponding to a power law model with $\Gamma \approx 1.7$ and a combined blackbody and power law model. These models qualitatively correspond to those of a low-state and high-state X-ray binary. Since we do not know the proper normalization between the blackbody and power law components for high-state objects (it varies from source to source), we tested whether each of the components separately, e.g. blackbody or a steep power law, could be distinguished from the simulated “low-state” spectrum. We chose to simulate spectra in *XSPEC* using the command *fakeit none*. We used generic response and ancillary response matrices. Simulating a power law model with a $\Gamma = 1.7$, we found that for 200, 400, and 1000 counts, these models were distinguishable at $> 99\%$ confidence from a blackbody source (with kT constrained to the range of 0.6 to 1.3 keV, similar to that of Galactic black holes). We found that the distribution in Γ values increases to a larger range for lower counts. Simulating a power law with $\Gamma = 2.5$, we find the same trend. We determined that at roughly 400 counts the distributions of Γ become entirely separable at $> 99\%$ confidence.

In order to distinguish between the different spectral fits for objects with $L_X \sim 2 \times 10^{38}$ erg s $^{-1}$, we select all galaxies that were observed for at least 10 ks (with the exception of the bright ULX in NGC 5408, which had enough photons for analysis despite the low exposure time) with *XMM-Newton* and that are closer than 8 Mpc. We estimated that these criteria would give us a minimum of 400 counts for objects with $L_X > 2 \times 10^{38}$ erg s $^{-1}$. We emphasize that the criteria quoted, based on the simulations, were used as a guide in choosing the sample of galaxies examined in this study. These simulations are not used as the statistical basis for our object-by-object analysis (discussed in Section 3).

Our sample of galaxies is selective in that it represents objects of interest in the X-ray band. We include details on these host galaxies in Table 1. *XMM-Newton* spectral information of individual X-ray sources had previously been published for approximately 60% of the host galaxies. We include references in the alternate ID column and footnotes of Table C1. We do not compare our results with these previous studies on a source by source basis.

We found that abstracts describing the proposals for *XMM-Newton* observations were available for only 13 of the 32 galaxies examined. Of these 13, only one observation cited the motive as a study of ULXs (NGC 1313). However, 7 of the remaining 19 galaxies contained sources classified as IXOs, intermediate X-ray objects, by Colbert & Ptak (2002). If the remaining galaxies were not studied due to their ULX population, the effects of bias are small with roughly 25% of the sources studied explicitly due to their connection with ULX sources. Our host galaxies include only spirals and irregulars. Figure 1 displays the distribution of galaxy type.

We reduced the data using the *XMM-Newton* Science Analysis System (SAS) version 6.0.0.

Since the processed pipeline products (PPS) were created with earlier versions of SAS, the observation data files (ODF) were used to produce calibrated photon event files for the EPIC-MOS and PN cameras using the commands *emchain* and *epchain*. Following this, the events tables were filtered using the standard criteria outlined in the *XMM ABC Guide*. For the MOS data (both MOS1 and MOS2 cameras), good events constitute those with a pulse height in the range of 0.2 to 12 keV and event patterns that are characterized as 0-12 (single, double, triple, and quadruple pixel events). For the PN camera, only patterns of 0-4 (single and double pixel events) are kept, with the energy range for the pulse height set between 0.2 and 15 keV. Bad pixels and events too close to the edges of the CCD chips were rejected using the stringent selection expression “FLAG == 0”.

Time filtering was applied as needed by editing the light curve produced in *xmmselect* for the entire observation. Flare events (distinguished by their high count rate) detected in all three cameras, were cut using the *tabgtigen* task as outlined in the *ABC Guide*. Typical count rate parameters for filtering were ‘RATE < 5’ for MOS detectors and ‘RATE < 20’ for the PN detector. Such filtering was only done as needed. Pre-filtered exposure times are listed in Table 1. The number of counts from the filtered net exposure times for the individual sources are listed in Table C1. We note that the filtered data are not always sufficiently clean that a high signal-to-noise is maintained up to 10 keV. Sources with a high background flux level, relative to the source spectrum, show poorer signal-to-noise in the spectrum above 1 keV.

Before extracting spectra of the brightest sources, contour maps of the X-ray observation were overlaid on Digital Sky Survey (DSS) images. This ensured that bright foreground stars and background AGN were easily distinguished, and thereby not included in our sample. Also, we checked the *XMM-Newton* source positions with NED and SIMBAD to determine if they coincide with any known background galaxies or QSOs. A list of these bright fore-ground or background sources is included in Table C2.

3. Spectral Fitting

Spectra for the bright point sources were extracted based on their apparent brightness in the CCD images. No explicit source detection algorithm was necessary. We used the SAS task *especget*. With this task we created spectra (for both the source and background), response matrices, and ancillary response files for all three EPIC cameras, when possible. The typical extraction radius was 20 arcseconds, but depending on both the size and proximity of a source to another source, the extraction radius ranged from 9 - 87 arcseconds. Background spectra were extracted either in an annulus centered on the source, or in a circle of appropriate size away from the source, depending on the proximity of the candidate source to other X-ray sources. Annuli were used for sources that were not located within a few arcseconds of another source, thus annular background extraction radii were not used for sources with small extraction radii. For sources in crowded regions, we used circular extraction radii close to the source. We extracted backgrounds close to the source in order to correct for emission local to the ULX. Once the spectra were obtained, they were rebinned to

require at least 20 counts per bin, using the command *grppha* in LHEASOFT. The list of sources, with position and count information, is included in Table C1. We only included sources for our spectral studies that had 400 or greater PN counts (or MOS for sources in NGC 253 and M81 and NGC 4945 XMM3 and NGC 2403 XMM1, for which PN spectra were not available)..

The extracted spectra were fit with standard models in XSPEC v11.3.1. For each source, we fit the PN and MOS spectra simultaneously in the 0.3-10 keV range. We allowed a free normalization constant to account for the differences in flux calibration between the three cameras (similar to Jenkins et al. (2004)). Each source was first fit with an absorbed single component model. In all cases we used the standard absorption model *wabs*, leaving the column density as a free parameter. For those sources where the hydrogen column density was unconstrained, we fixed the value to the Galactic foreground value listed in Table 1. Results of the single-component fits are seen in Table 2. We include in this table only the best-fit parameters for those sources best described by a single-component model. The flux values quoted represent the unabsorbed flux in the PN spectra, in the 0.3-10 keV band. All errors quoted, here and subsequently, correspond to the 90% confidence level for one degree of freedom ($\Delta\chi^2 = 2.71$). The luminosities were calculated from the unabsorbed flux using the distances quoted in Table 1. Both flux and luminosity correspond to those of the best fit model (power law or bremsstrahlung). It should be noted that since our selection criteria was based on a count rate cutoff, due to the variety of spectral forms, the inferred luminosity cutoff will not be uniform.

In Table 2 we denote the single component model we choose as the better fit in bold. This notation also indicates the model (power law or bremsstrahlung) used to compute the quoted flux. For $\approx 46\%$ of the power law sources, the χ^2 difference (< 2) between the power law and bremsstrahlung models is only marginally different. Of these sources, the average kT value for the bremsstrahlung fit is 5.54 keV. From our simulations we find that at high temperatures the bremsstrahlung fit becomes indistinguishable from a simple power law. Thus, given the high temperatures of the bremsstrahlung fits for these sources, they are equally well described by the power law model. Typical kT bremsstrahlung values for accreting neutron stars are from 3.0 to 7.0 keV (Jones 1977).

For a number of sources, we found that an improvement in reduced χ^2 (sources with $\Delta\chi^2 < 2.3$, corresponding to $\approx 68\%$ confidence using the F-test for two degrees of freedom, are listed in Table 2) was achieved through fitting their spectra with an absorbed two-component blackbody and power law model. We chose a simple blackbody model over the multi-component disk model, *diskbb*, for purely schematic reasons. Namely, observations of galactic X-ray binary systems were fit with blackbody models in the 1980s, when the signal-to-noise of these objects was comparable to that for our *XMM* data for ULX sources. We also note that the *diskbb* model does not give an entirely accurate physical description of the data as it neglects the effects of general relativity. As a schematic model, the blackbody model is simpler than *diskbb*, with the same number of degrees of freedom. In addition, for low temperatures both models yield virtually identical temperatures. For this study, we chose the simpler model. We defer to a further paper a discussion of the different

models for the thermal component.

In Table 3 we present the results for the sources which are fit significantly better by the two-component model. We include the improvement in χ^2 of the two-component fit over the simple power law. We include the power law best fits to these sources in the appendix for comparison with other analyses. In order to determine whether the blackbody component is statistically significant for the sources fit with a two-component model, we simulated spectra based on accurate modeling of some of the brightest sources: NGC 247 XMM1, NGC 5408 XMM1, and Holmberg II XMM1. These sources span the observed range of the ratios of the blackbody to power law component and thus represent those from our sample with a weak blackbody relative to the power law component, intermediate case, and a strong blackbody, respectively. Our simulations are described in full in Appendix A. We found that, using a $\Delta\chi^2 > 8$ criterion, which corresponds to the 99% significance level as according to the F-test for the addition of two extra parameters, we can readily detect the the strong and intermediate thermal components in all spectra with more than 400 counts. The weak thermal emission cannot be detected in 400 count spectra, but is readily detected in 2000 count spectra. This gives us confidence that our results are statistically meaningful.

In Table 4, we list sources that have $\Delta\chi^2$ values less than 8 for a single observation. Most of these sources have weak blackbody normalizations compared to the power law normalization. We classify these sources as being well-fit by a two-component model while acknowledging the uncertainty in the fit as determined by the simulations. The addition of the thermal component is not significant enough for these sources to be classified with certainty in either Table 3 or 4. The simple power law fits for these sources are included with those for sources in Table 3 in the appendix. We note that due to their high luminosity we included four of these sources (NGC 4490 XMM3, M51 XMM2, M51 XMM6, and M101 XMM3) with uncertain fit parameters as ULX high-state sources. Two of these sources (NGC 4490 XMM3 and M51 XMM6) had unabsorbed luminosities > 10 times the 3×10^{39} erg s $^{-1}$ cutoff used for high-state ULX classification. The other two sources had luminosities above the threshold, as well as weak blackbody components compared to the power law (see the appendix for simulations). We used these points to justify including these sources with the Table 3 sources in the following discussions with the proviso that their spectral fits do not indicate absolutely the necessity of the additional thermal component. For this reason, we denote these sources with a special symbol in subsequent figures while including them as “high-state” objects (see classification information in Discussion section).

For those sources we classify as ULXs (see section 4.1 for our criteria), we computed bolometric luminosities. We used the exponentially cutoff power law spectrum of Magdziarz & Zdziarski (1995), model *cutoffpl* in *XSPEC*, with a cutoff energy of 10 keV. From observational studies of Galactic X-ray binaries, it has been observed that low-state objects have spectra that cut-off at high energies ($\gtrsim 10 - 200$ keV) (Zdziarski & Gierlinski 2004). Thus we chose the exponential model *cutoffpl* over a simple power law. This also minimizes the total luminosity for flat power law sources. We computed an unabsorbed flux in the 0.1 – 100 keV range through use of the *dummyresp* command (which extends the model beyond the observation’s energy range). The luminosity was then computed

using the distances listed in Table 1. We quote these values as $L_{cutoffpl}$ (the luminosity obtained from extrapolating the power law portion of the spectrum as an exponentially cut-off power law) in Table 5. We note that these values represent an upper limit on the bolometric luminosity for steep power law ($\Gamma > 2$) objects, since we would expect the power law component to cutoff at some low energy. However, for shallow spectrum ($\Gamma < 2$) sources L_{pow} is a lower limit. This is because, schematically, a steep power law diverges from the blackbody at low energies while a shallow power law diverges from the blackbody at high energies.

For our ULX sources modeled by a combined blackbody and exponentially cutoff power law, we estimate a more accurate L_{bol} , calculated from the flux in the range of $2 \times kT - 100 \text{ keV}$ where kT is the blackbody temperature obtained from the model. In galactic X-ray binary systems, the power law component of the X-ray spectrum is believed to be from Comptonization in a corona. The photons supplying this energy originate from the blackbody continuum emanating from the accretion disk. Thus, a natural cutoff for this power law component occurs at the peak emission of the blackbody (which is approximately $3 \times kT$). The estimated values (obtained from cutting off the combined unabsorbed blackbody and cutoff power law model at the value $2 \times kT$) differ with regard to the full estimate (flux from the fully integrated blackbody added to the separate flux from the cutoff power law from $3 \times kT$ to 100 keV) depending on the normalization factors used (for both the blackbody temperature and the spectral index Γ). Choosing three sources displaying a range of blackbody to power law strength (Holmberg II XMM1, NGC 253 XMM1, and IC 0342 XMM3) we found that the estimated values were within 88.3, 95.1, and 96.8% of the more complete estimation. Given their close proximity (within approximately 90%) we quote these estimated values as a good approximation to the bolometric luminosity.

We note that our bolometric luminosities, on average, are a factor of 1.08 greater than the X-ray luminosities in the $0.3 - 10 \text{ keV}$ band for the objects best fit by a combined blackbody and power law. Thus, to good approximation, the X-ray luminosity is the bolometric luminosity. However, for the objects best fit by a simple power law, the average bolometric luminosity is roughly a factor of 7 greater than the X-ray luminosity in our band. This average is dominated by the steep power law objects, in particular Holmberg II XMM1 ($\Gamma = 3.09$). Excluding this object, we get an average bolometric luminosity that is 2.8 times the X-ray flux and more indicative of the general properties of these power law-fit objects.

In addition, in this large sample of point sources, we came across a number of objects whose spectra were not well fit by the models we employed. We briefly describe these sources in the appendix.

4. Discussion

We have determined best-fit spectral parameters of the bright X-ray sources in 32 nearby galaxies. In choosing three “standard” models for our study, we hoped to accurately separate

high and low state ULXs from other types of luminous X-ray sources. We specifically chose to fit the data with the bremsstrahlung model in order to identify neutron star X-ray binaries within our sample. The models we used are purely schematic, and they do not physically explain the phenomena occurring, but are standard and qualitatively simple models often used to fit the spectra of Galactic X-ray binaries.

We cross-referenced the X-ray positions of our sources with both NED and SIMBAD in order to identify known supernovae, galaxies, and stars. In addition, we examined the DSS optical images to place the position of our sources within their respective galaxies. Such analysis aimed to minimize contamination of our sample of ULXs with bright background and foreground sources.

Further, we examined *XMM-Newton*'s Optical Monitor data in the visual bands (U, B, V). The *XMM* PPS contain point source detection files for the OM data. We overlaid these point source detections with X-ray contour maps in order to determine the **brightest possible** optical count rates for the X-ray sources, which were then converted into fluxes using the OM calibration documentation. In Figure 2, we plot the distribution of the logarithm of the X-ray to optical flux for the brightest possible optical counterpart inside the *XMM-Newton* error circle. Only 13 of the 32 host galaxies had visible band OM data during the observations. Of these 13 galaxies, 40 of the X-ray sources were in the range of the OM data and only 14 were coincident with an optical point source. Therefore, the majority of our sources have X-ray/optical flux ratios that are **larger** than those displayed. Figure 2 illustrates the lowest possible X-ray/optical flux ratios and also, by the sparsity of sources included in the diagram, it illustrates the fact that a majority of the sources have no obvious optical counterpart and thus have very large X-ray/optical flux ratios. We estimate the point source detection limit of the OM U filter as approximately 1.24×10^{-14} erg cm $^{-2}$ s $^{-1}$. For an unabsorbed X-ray flux of 1.0×10^{-12} erg cm $^{-2}$ s $^{-1}$, typical of objects with $L_X \approx 2 \times 10^{38}$ erg s $^{-1}$ located at a distance of 8 Mpc, this corresponds to $\log(f_x/f_{opt}) = 1.9$. Therefore, the average value for our sources should fall around 2 or greater. The average distribution for QSOs and AGN centers around 0 and 0.8 for BL Lacs (Anderson et al. 2003). Our objects have ratios of L_x/L_{opt} at least 10 times higher than those of AGN and 100 times greater than stars.

Recently, Gutierrez & Lopez-Corredoira (2005) identify six ULXs from the catalog of Colbert & Ptak (2002) as QSOs. They hypothesize that a large number of ULXs may in fact be quasars at higher redshift than their supposed host galaxy. However, unlike the objects studied in Gutierrez & Lopez-Corredoira (2005), our ULX sources are all spatially coincident with the optical host galaxy. In addition, a majority of our ULXs are not in the proximity of a noticeable optical point source. The X-ray/optical flux ratios of our sources are much larger, on average, than might be expected for a QSO. It is also worth noting that while some catalogued ULXs may be QSOs, optical identifications have been made associating other ULXs with a type B supergiant companion (Kuntz et al. 2005; Liu et al. 2004).

4.1. Classification Criteria

The spectral fits indicate that to high statistical probability (see appendix A) we can distinguish a class of low-state ULXs from the high-state objects. As a constraint on our ULX classification, we require our X-ray sources to clearly coincide with the optical extent of the host galaxy (as determined from the DSS images). Of the sources in Table 2, 16 are “low-state” objects, having unabsorbed luminosities $> 10^{38} \text{ erg s}^{-1}$ and spectra that are well fit by power law models. With these sources we include both “low-state IMBH candidates” (sources with $L_X < 3 \times 10^{39} \text{ erg s}^{-1}$) and “low-state ULXs”, as listed in Table 5, referring to both generally as low-state ULXs. In the Spectral Fitting section, we noted that a power law and high temperature bremsstrahlung model are indistinguishable. Therefore, it is important to consider the luminosity of these sources in the claim that they are not neutron star X-ray binaries accreting at the Eddington luminosity. Of the low-state ULX sources, only two of the 16 sources have bolometric luminosities below the Eddington luminosity of a $3 M_\odot$ object ($\approx 4 \times 10^{38} \text{ erg s}^{-1}$), corresponding to the maximum mass of a neutron star. All of the sources have values exceeding the Eddington limit for a $2 M_\odot$ neutron star.

Further, 26 sources have unabsorbed $L_X > 3 \times 10^{39} \text{ erg s}^{-1}$, corresponding to $L \approx L_{Edd}$ at $M > 20 M_\odot$ as expected for “high-state” IMBHs, and spectra that are well fit by combined blackbody and power law models. These are “high-state” objects. In a statistical sense, we find that the greater the number of counts in the observation the greater our confidence in the thermal component contributing to a better fitting model. We explain our confidence levels obtained from spectral simulations in the appendix.

In addition to these high and low state ULXs, we find a large number of sources best fit by a combined blackbody and power law model but below our threshold of $L_X = 3 \times 10^{39} \text{ erg s}^{-1}$ for a high-state ULX. Many of these sources may be accreting stellar mass black holes with $M < 20 M_\odot$. Some of these non-“ULX” sources were found away from the optical extent of the targeted galaxy (from our analysis of the DSS images), and therefore may be background AGN.

4.2. Low-State ULX

For Galactic black hole X-ray binaries, spectral indices of low-state objects are typically lower than those of high-state objects with $< \Gamma >_{low} \approx 1.7$ and $< \Gamma >_{high} \approx 2.5$ (McClintock & Remillard 2004). In Figure 3, we plot the distribution of the spectral index for both high-state and low-state objects. The spectral index for the high-state objects is the value of Γ from the two-component fit. As in the Galactic sources, it is clear that the spectral indices of the high-state objects are indeed larger. Of further interest, the distribution of spectral index for low-state objects looks remarkably similar to the distribution of spectral index for moderate luminosity quasars, many of which are thought to be the analogs of low-state black holes (Porquet et al. 2004). This supports the classification of these objects as accreting black holes.

For the high-state objects, we find mean values of $\Gamma = 2.46$, with a root mean square (rms) deviation of $S = 0.12$, and $L_X = 1.4 \times 10^{40} \text{ erg s}^{-1}$, $\log(S) = 1.6$. This calculation excludes the 3 objects with spectral indices greater than 3.5. For the low-state objects, we find mean values of $\Gamma = 2.09$, with a rms deviation of $S = 0.10$, and $L_X = 2.2 \times 10^{39} \text{ erg s}^{-1}$, $\log(S) = 2.1$. This value of $\Gamma = 2.1$ is softer than the typical hard-state value of ≈ 1.7 , but within the $1.5 < \Gamma < 2.1$ range used to classify this state for Galactic X-ray binaries (McClintock & Remillard 2004). Computing a Kolmogorov-Smirnov two-sample test, separating the sources into the category of low-state or high-state, we find a likelihood of approximately 0.03 that the spectral indices belong to the same distribution.

The low hard X-ray state of X-ray binaries is associated with a low accretion rate from the companion object with $L \lesssim 0.1 L_{Edd}$ (Done & Gierlinski 2003). Therefore, on average, we expect the luminosities of the low-state objects to be lower than the high-state objects. Figure 4 displays the luminosity of the objects as a function of the spectral index. On average, the highest luminosity low-state objects have luminosities lower than those of the high-state objects.

The lower L_X values of the low-state objects imply that they may indeed be accreting at a lower rate than the high-state objects. This can further be seen in the bolometric luminosities listed in Table 5. If these objects are accreting at a rate similar to galactic low-state black holes ($0.1 \times L_{Edd}$) (Done & Gierlinski 2003), we can estimate their masses as

$$\frac{M}{M_\odot} = \frac{L_{bol}}{0.1 \times L_{Edd}}$$

with L_{Edd} as the Eddington luminosity for a $1 M_\odot$ object ($1.3 \times 10^{38} \text{ erg s}^{-1}$). Our mass estimations, based upon our limits to the bolometric luminosities, yield masses of $20 - 1500 M_\odot$ (see Table 5), precisely what we might expect for a population of IMBHs.

4.3. High-State ULX

If the high-state ULXs represent a class of intermediate mass black hole systems, their X-ray spectra should be well described by a combined blackbody and power law model. Scaling for the mass of the black hole, we would expect a relationship of $T \propto M^{-1/4}$ between black hole mass and blackbody temperature (Makishima et al. 2000). This would indicate a thermal component of $\sim 100 \text{ eV}$ for masses of $\sim 10^3 M_\odot$. A few objects have been reported to display this property (Miller et al. 2003; Roberts et al. 2005). In Figure 5, we graph the distribution of the thermal component for our classified high-state objects.

We find that there are two peaks in the distribution among the thermal component, one at approximately 100 eV and another centered close to 1 keV. This could indicate two different classes among the high-state objects. It is possible that those objects with blackbody components near 100 eV are indeed high-state intermediate mass black holes. We note that the soft excess in PG Quasars has also been modeled as a blackbody with $kT_{soft} \approx 100 \text{ eV}$, but it has been suggested

that this could be the result of a process not directly related to black hole accretion (such as the presence of a warm absorber: Gierliński & Done (2004)). Another possible explanation is that the soft component is the result of ionized reflection from the disk (Ross & Fabian 2005). While the possibility exists that the “thermal” component of these 100 eV sources is not directly related to black hole accretion or is related in a “non-thermal” (i.e. ionized reflection) sense, as may be the case with the soft excess in PG Quasars, we assume that the soft component for the objects we classify as high-state ULXs originates from a thermal disk. We use this assumption to test the IMBH hypothesis, thus speculation on the nature of the soft component is beyond the scope of this paper.

The second peak, centered around 1 keV, has a temperature reminiscent of the Galactic black hole systems in our own galaxy. These systems may thus be stellar-mass black holes accreting matter near the Eddington limit. If this were the case, we would expect the luminosities of the sources exhibiting a higher blackbody temperature to be lower than those with cooler blackbody components. In the second graph of Figure 5, we plot the relationship between blackbody temperature and L_X in the 0.3 - 10 keV band. Once again, two classes of ULXs are seen. The most luminous objects are those with low blackbody temperatures. On average, the less luminous sources exhibit higher blackbody temperatures. For the sources with $L_X > 10^{40}$ erg s $^{-1}$, the mean blackbody temperature is 0.31 while the sources below this luminosity threshold have a mean blackbody temperature of 0.61.

The second, low-luminosity, class of ULX is clearly distinguishable in both plots of Figure 5. We found that, with the exceptions of NGC 253 XMM1, M81 XMM1, and NGC 5204 XMM1, the spectra of these objects could also be well-described by an absorbed Comptonization (*compST*) model (Sunyaev & Titarchuk 1980) used to fit galactic black holes in the “very high” state when they are radiating at the Eddington limit. This model simulates Compton scattering of cool photons on the hot electrons of a completely ionized plasma. We present the best-fit parameters for the Comptonization model in Table C4.

This “very high” state has been observed (Miyamoto et al. 1991) in a few Galactic black holes. Yet another rubric for the very high state emerged in Kubota et al. (2001) and Kubota & Makishima (2004), where they identify this as the “anomalous” state, a state whose spectrum can be well fit by a Comptonized scattering model. Regardless of the name, our best-fit Comptonization sources likely fit into this category. The luminosities of these sources suggest that they are stellar mass black hole systems in this anomalous/very high state.

As with the low-state, we include mass estimates for our high-state objects in Table 5. We assume that the high-state objects are radiating at L_{Edd} resulting in a minimum mass if there is no beaming. We find masses of $1.6 - 38 M_\odot$, consistent with “normal” stellar mass BHs, for the sources well fit by the Comptonization model. The other high-state ULXs masses range from $17 - 1350 M_\odot$ based on Eddington rates, analogous to the low-state ULX masses computed.

It is important to note that the initial simulations (appendix) and discussions in the Spectral

Simulations section need to be considered in relation to the impact they pose to our classification scheme and the results presented in these sections. While it is indeed possible that some of the objects with a weak blackbody component and a relatively small number of counts would be mis-categorized as a pure power law spectrum, one can ask what such a possible situation would do to the correlations that we have seen. These putative objects, by assumption would have lower luminosities, however their temperatures are unknown and it is entirely unclear if they would destroy the $kT/L(x)$ correlation. As we have shown in our simulations it is unlikely that the fitted power law index would change and thus the presence of a low state as indicated by the spectral index would not change. This would create a new type of object, one with a flat power law and a black body component, which is not seen in the Milky Way, nor among the high signal to noise objects.

4.4. Temperature Gap

In addition to the existence of ULXs with low blackbody temperatures, the temperature distribution (Figure 5, left panel) displays a “gap” which is of particular interest — there is a complete absence of objects with temperatures in the range 0.26 keV to 0.50 keV. It is tempting to take this as evidence for a gap in the mass distribution of these accreting black holes. Since, for a given luminosity, we expect the temperature to vary as $T \propto L^{1/4}M^{-1/2}$, this factor of two gap in the temperature distribution translates into a factor of four gap in the black hole mass distribution.

If this result is borne out by further study, it provides an important clue to the origin and evolution of intermediate mass black holes. One popular idea is that intermediate mass black holes formed from the collapse of massive Population III stars (Madau & Rees 2001). Models suggest that Pop III stars with zero age main sequence (ZAMS) masses in the range $25\text{--}140M_{\odot}$ and above $260M_{\odot}$ collapse to produce black holes (Heger & Woosley 2002) whereas in the range of ZAMS masses $140\text{--}260M_{\odot}$, pair-instability supernovae lead to the complete disruption of the stars (i.e., no remnant black hole remains). Hence, this model for IMBH formation predicts a gap in the IMBH initial mass function in the range of approximately $60\text{--}200M_{\odot}$ (although this is uncertain on the low end due to the effect of the pulsational pair-instability on the pre-collapse core). One possibility is that the gap in our observed temperature distribution (and hence the inferred gap in the mass function) is due to this effect of the pair instability supernovae in Pop III stars. This would require that the current IMBH mass function is approximately the same as the initial IMBH mass function. In other words, it requires that most IMBHs (especially those just below the gap) have not grown significantly due to accretion since their formation and, hence, that the ULX phase represents a short fraction of the life-time of an IMBH ($f \ll t_{\text{sal}}/t_{\text{H}}$, where $t_{\text{sal}} \approx 45\epsilon_{0.1} \text{ Myr}$ is the e-folding timescale for Eddington limited black hole growth with radiative efficiency $\epsilon = 0.1\epsilon_{0.1}$).

An alternative interpretation of the inferred mass gap is to suppose that two fundamentally different modes of formation lead to a strong bi-modality in the final black hole mass function. Black hole masses below the gap can be readily understood through normal stellar processes. A

separate and distinct population of significantly more massive black holes may result from dynamical processes in the core of dense globular clusters (Miller & Hamilton 2002; Gltekin, Miller, & Hamilton 2004).

4.5. Galactic HMXBs

Supposing that the Galaxy’s bright X-ray population is representative of low-redshift galaxies, we expected to find a number of sources similar to Galactic X-ray binaries in our sample. In our sample, we find approximately 24 sources with luminosities below our high-state ULX cutoff ($\approx 3 \times 10^{39} \text{ erg s}^{-1}$), X-ray positions within the optical extent of their host galaxy, and no obvious optical counterpart. The unabsorbed luminosities for these sources range from $0.4\text{--}2.5 \times 10^{39} \text{ erg s}^{-1}$ (0.3 – 10 keV band). Two of these sources were transients in the *XMM* data. Of the four host galaxies with multiple observations examined, two of these galaxies contained solely ULX sources in our luminosity regime (Holmberg II and NGC 5204). Each of the remaining two (NGC 253 and NGC 4258) had a transient source best fit by a combined blackbody and a power law.

This suggests an interesting diagnostic in terms of distinguishing our ULX sources from a normal HMXB population. In our own galaxy, most HMXBs vary on timescales of days or less and most of the black holes in the Milky Way are transients, though some HMXBs are indeed persistent. The figures in Kalogera et al. (2004), determined through detailed mass-transfer calculations, indicate that transient behavior should not be expected from a population of IMBHs. Thus, on average, our ULX sources should remain X-ray bright in multiple observations. Through a literature search, we found that 37/42 of our ULX sources are well detected in ROSAT observations and thus are luminous for greater than 10 years and therefore are not transients. Examination of the long term light curves show that most of these sources vary by less than a factor of 3 over the timescale from ROSAT to XMM. The sources that have been above the Eddington limit in the Milky Way and the Magellenic clouds do so transiently, for a small fraction of the time. As best as we can tell, from the light curves from Einstein, ROSAT, ASCA, Chandra and XMM the ULXs are, rarely, transients, and are almost always ‘on’, unlike Galactic “ultra-luminous” objects.

As a possible further diagnostic, we constructed a color-color diagram for our ULX sources. We adopted the colors of Done & Gierlinski (2003) in order to compare our sample with their sample of Galactic X-ray sources. Thus, our colors were constructed from unabsorbed **model** fluxes in four energy bands: 3-4, 4-6.4, 6.4-9.7, and 9.7-16 keV. The *XSPEC* command *dummyresp* was used to calculate a flux based on the model for the 10-16 keV range. We plot colors for a pure unabsorbed power law (from $\Gamma = 1.5\text{--}3.0$) and an unabsorbed MCD model (*diskbb* in *XSPEC* with $kT_{in} = 5.0\text{--}0.2 \text{ eV}$) for comparison. Comparing our Figure 6 with Figure 8 of Done & Gierlinski (2003), we find that our ULX sources largely lie along the same regions as their black hole sources. A few ULX sources, however, lie in the region occupied by atoll and Z-sources in the plot of Done & Gierlinski (2003). These sources were those best fit by a Comptonization model.

4.6. Galaxy Sample

It has been shown that the ULX population is proportional to the host galaxy's star formation rate (SFR) (Ranalli et al. 2002; Grimm et al. 2003). The far-infrared luminosity of a galaxy is used as an indicator of the SFR. In order to compare the ULX population of a galaxy with the SFR we followed a similar approach to Swartz et al. (2004). We calculate the FIR flux from observations taken by the *Infrared Astronomical Satellite*. As in Swartz et al. (2004), the flux between 42.4 and 122.5 μm is approximated as $1.26 \times 10^{-11} (2.58S_{60} + S_{100}) \text{ erg cm}^{-2} \text{ s}^{-1}$. The values of the flux at 60 μm (S_{60}) and 100 μm (S_{100}) were obtained from either Ho et al. (1997) or NED. Luminosities were calculated using the distances quoted in Table 1. We list these values in addition to the number of ULXs observed in individual galaxies in Table C5. The number of ULXs includes both the objects we classify as high and low state ULX as well as those sources resolved by Chandra.

In Figure 7, we show two plots relating the number of ULXs to L_{FIR} . It has been suggested by Grimm et al. (2003) that the luminosity function in the X-ray regime from HMXBs is related to SFR. In our first plot, we find that the galaxies with the highest L_{FIR} seem to have fewer ULXs than may be expected from the luminosity functions of Grimm et al. (2003), who present a relationship showing a scaling of the number of HMXBs with luminosities over a set threshold with the host galaxy's SFR (see equation 7; Grimm et al. 2002). Using this relationship, we would expect that a galaxy with a SFR approximately equal to that of M51 ($\approx 4 M_{\odot} \text{ yr}^{-1}$ from their table 1) to have ≈ 4.47 objects with luminosities greater than $10^{39} \text{ erg s}^{-1}$. We find 5 objects with this luminosity in M51, consistent with their result. However, for NGC 4945, a galaxy with approximately the same L_{FIR} and therefore SFR, we find only one source with a luminosity in this range. However, we note that NGC 4945 is a Seyfert, implying that the L_{FIR} may primarily be caused by the AGN and not a direct indication of SFR. In addition to high L_{FIR} sources with few ULX we find a number of sources with very small SFR but which contain a ULX. For sources with $\text{SFR} < 0.2 M_{\odot} \text{ yr}^{-1}$, which corresponds roughly to sources with L_{FIR} less than that of NGC 4736, we would expect < 0.22 sources with luminosities above $10^{39} \text{ erg s}^{-1}$. However, there are a number of bright ULX in galaxies with very low SFRs (for instance Holmberg II, Holmberg IX, NGC 5204, and NGC 5408). Thus, in a direct comparison, our results do not agree with the predictions of Grimm et al. (2003).

The second plot displays the average number of ULXs/galaxy, binned according to luminosity. This plot is extremely similar to Fig. 15 of Swartz et al. (2004) for spiral galaxies. Thus, once again, it seems that the connection between SFR and the ULX population in spirals is supported. For irregular galaxies, however, there seems to be more of a spread in the distribution. This could be the result of poor sampling — most of the bins contain only one galaxy. Another possibility is that there is no direct correlation in irregular galaxies or that the overall star formation in these galaxies is less ordered or clumpier. If the latter is the case, the overall SFR of the galaxy is only an average over a wide range of values. We shall address this issue again in the next paper in this series (L.M. Winter et al., in preparation) where we discuss the local environments of the ULXs in our sample.

In Figure 8 we plot the distribution of column densities among the ULX. We subtracted the Galactic column density towards the galaxy (obtained from the nH FTOOL and listed in Table 1) from the values obtained through spectral fits. We note that, on average, the ULXs have large column densities. The typical Galactic column density along a line of sight is $\approx 4 \times 10^{20} \text{ cm}^{-2}$. If the ULX is located on the opposite side of its host galaxy, we might expect maximum column densities of $\approx 1.2 \times 10^{21} \text{ cm}^{-2}$. However, most of our sources have column densities well above this value. This is in agreement with the analysis of 5 ULXs by Roberts et al. (2004) and may imply, as they suggest, that the local environment of the ULXs contains an extra source of absorption. We are investigating this further, comparing the X-ray absorption column densities with HI data (L.M. Winter et al., in preparation).

In order to better understand the relationship between SFR and the ULX population, it is necessary to extend ULX studies to other wavelengths. In particular, it becomes important to analyze UV and IR images close to the ULX.

5. Conclusion

We have found from our *XMM* survey of the ULX population in nearby galaxies that there exists a population of objects whose X-ray spectral properties closely match the low-state spectra of Galactic black holes, but whose luminosities lie in the range of $L_{bol} \approx 2 \times 10^{38} - 1 \times 10^{40} \text{ erg s}^{-1}$. In the Milky Way, black holes with these spectral properties radiate at only ≈ 0.05 of the Eddington limit. If this is also true for this population, it indirectly implies that these objects have a mass greater than $\approx 30 M_{\odot}$ ranging up to $1500 M_{\odot}$ and thus should be IMBHs. The existence of such objects was “predicted” on the basis that the ULXs previously studied shared the X-ray spectral characteristics of high-state Galactic black holes; namely, an X-ray spectrum best fit by a combined blackbody and a power law (Miller et al. 2003), but with much higher luminosities. If these objects are high-state IMBHs, the corresponding low-state objects should also exist.

Our survey has also uncovered a large population of objects whose X-ray spectra are well modeled by the canonical description of Galactic black holes in the high-state, a black hole with a steep power law, but whose bolometric luminosities exceed $2 \times 10^{39} \text{ erg s}^{-1}$, ranging up to $10^{41.5} \text{ erg s}^{-1}$ and whose blackbody temperatures are less than 0.3 keV. If these objects are radiating at $\approx 1/2$ the Eddington limit like their Milky Way counterparts their implied masses are from $30 - 3000 M_{\odot}$, a range very similar to that implied by the low-state objects. Using the $M^{-1/4}$ scaling of mass to temperature, the observed spectral temperatures give masses of $500 - 10^4 M_{\odot}$ a considerably larger value. In general agreement with the expectations of the IMBH hypothesis, the objects with high-state spectra are more luminous than those with low-state spectra.

The existence of a substantial population of ULXs in nearby dwarf and other low star formation rate galaxies argues that (in agreement with Ptak & Colbert (2004); Swartz et al. (2004)) there is more than one source term for the origin of ULXs, with at least some of them not being associated

with recent star formation, at least statistically. We note that these results have required the high signal to noise of *XMM* in order to discern the spectrum of these objects. Many of these objects have also been observed by Chandra and their spectra have been well-fitted by simple power laws.

We conclude, from an X-ray spectral and luminosity point of view, that our data are consistent with many of these objects having the properties expected of an IMBH population. However, we also find two other populations of objects, those whose blackbody temperature and luminosity correspond to that of stellar mass black holes with $kT \approx 1 \text{ keV}$ and $\log L_X$ less than $2 \times 10^{39} \text{ erg s}^{-1}$ and a small population of objects whose X-ray spectra and luminosities are consistent with that of stellar mass black holes in the very high state. Thus, ULX selected purely on the basis of $0.3 - 10 \text{ keV}$ X-ray luminosities are a composite class with $\approx 1/4$ being “normal” stellar mass black holes and the rest being consistent with a population of IMBHs.

In a follow-up paper we will discuss the environments of these objects as revealed by *XMM* OM UV imaging and the implications this has for the origin of ULXs.

L.W. gratefully acknowledges Kip Kuntz and M. Coleman Miller for helpful discussions. We would also like to acknowledge R. Narayan for asking the question “are there any low-state ULXs?” at the Kyoto Black Hole meeting.

REFERENCES

Anderson, S. et al. 2003, AJ, 126, 2209
Bauer, F.E., Brandt, W.N., & Lehmer, B. 2003, AJ, 126, 2797
Begelman, M. C. 2002, ApJ, 568, L97
Belloni, T., et al. 1997, ApJ, 488, L109
Brandt, W.N., Iwasawa, K., & Reynolds, C.S. 1996, MNRAS, 281, L41
Chen W., Schrader C. R., Livio M., 1997, ApJ, 491, 312
Colbert, E.J.M. & Ptak, A.F. 2002, ApJS, 143, 25
Done, C. & Gierlinski, M. 2003, MNRAS, 342, 1041
Ebisawa, K., et al. 2003, ApJ, 597, 780
Eracleous, M., Shields, J.C., Chartas, G., & Moran, E.C. 2002, ApJ, 565, 108
Freedman, W. L., et al. 1994, ApJ, 427, 628
Freeman, K. C., Karlsson, B., Lynga, G., Burrell, J. F., van Woerden, H., & Goss, W. M. 1977, A&A, 55, 445

Gierliński, M. & Done, C. 2004, MNRAS, 349, L7

Grimm, H.-J., Gilfanov, M., & Sunyaev, R. 2003, MNRAS, 339, 793

Guainazzi, M., et al. 2000, A&A, 356, 463

Gültekin K., Miller M.C., Hamilton D.P., 2004, ApJ, 616, 221

Gutierrez, C.M. & Lopez-Corredoira, M. 2005, preprint (astroph/0502290)

Hartwell, J., et al. 2004, MNRAS, 348, 406

Heger A., Woosley S.E., 2002, ApJ, 567, 532

Ho, L.C., Filippenko, A.V., & Sargent, W.L.W. 1997, ApJS, 112, 315

Humphrey, P.J., Fabbiano, G., Elvis, M., Church, M.J., & Balucinska-Church, M. 2003, MNRAS, 344, 134

Jenkins, L.P., Roberts, T.P., Warwick, R.S., Kilgard, R.E., & Ward, M.J. 2004, MNRAS, 349, 404

Jones, C. 1977, ApJ, 214, 856

Jonker, P.G. & Nelemans, G. 2004, MNRAS, 354, 355

Kaaret, P., Corebel, S., Prestwich, A.H., & Zezas, A. 2003, Science, 299, 365

Kalogera, V., Henninger, M., Ivanova, N., & King, A.R. 2004, ApJ, 603, L41

Karachentsev, I.D., Sharina, M.E., Dolphin, A.E., et al. 2002, A&A, 385, 21

Kelson, D. D. 1996, ApJ, 463, 26

King, A.R. et al. 2001, ApJ, 552, L109

Kong, A.K.H. 2003, MNRAS, 346, 265

Kong, A.K.H. & Di Stefano, R. 2003, ApJ, 590, 13

Kording, E., Falcke, H., & Markoff, S. 2002, A&A, 382, L13

Kubota, A. & Makishima, K. 2004, ApJ, 601, 428

Kubota, A. et al. 2001, ApJ, 560, L147

Kuntz, K. et al. 2005, ApJ, 620, L31

Lehmann, I. et al. 2005, A&A, 431, 847

Lira, P., Lawrence, A., & Johnson, R.A. 2000, MNRAS, 319, 17

Liu, J. F., Bregman, J. N., & Seitzer, P. 2004, *ApJ*, 602, 249

Madau P., Rees M.J., 2001, *ApJ*, 551, L27

Magdziarz, P. & Zdziarski, A.A. 1995, *MNRAS*, 273, 837

Makishima, K., et al. 2000, *ApJ*, 535, 632

Martin, C.L., Kobulnicky, H.A., & Heckman, T.M. 2002, *ApJ*, 574, 663

McClintock, J.E. & Remillard, R.A. 2004, preprint (astroph/0306213)

Miller, J. M., Fabbiano, G., Miller, M. C., & Fabian, A. C. 2003, *ApJ*, 585, L37

Miller, J.M., Fabian, A.C., & Miller, M.C. 2004, *ApJ*, 614, L117

Miller, M. C. & Colbert, E. J. M. 2004, *IJMPD*, 13, 1

Miller M.C. & Hamilton D.P., 2002, *MNRAS*, 330, 232

Miyamoto, S. et al. 1991, *ApJ*, 383, 784

Pietsch, W. et al. 2001, *A&A*, 365, 174

Pietsch, W., Haberl, F., & Vogler, A. 2003, *A&A*, 402, 457

Ptak, A. & Colbert, E. 2004, *ApJ*, 606, 291

Pakull, M.W. & Mirioni, L. 2003, *RMXAA*, 15, 197

Porquet, D., Reeves, J.N., O'Brien, P., & Brinkmann, W. 2004, *A&A*, 422, 85

Radecke, H.D. 1997, *A&A*, 319, 18

Reynolds, C.S., et al. 1997, *MNRAS*, 286, 349

Roberts, T.P. & Warwick, R.S. 2000, *MNRAS*, 315, 98

Roberts, T.P., Warwick, R.S., Ward, M.J., & Goad, M.R. 2004, *MNRAS*, 349, 1193

Roberts, T.P. et al. 2005, *MNRAS*, 357, 1363

Ross, R.R. & Fabian, A.C. 2005, *MNRAS*, 358, 211

Sakai, S., Madore, B.F., & Freedman, W.L. 1996, *ApJ*, 461, 713

Sakai, S. & Madore, B.F. 1999, *ApJ*, 526, 599

Schlegel, E.M., Petre, R., Colbert, E.J.M., & Miller, S. 2000, *AJ*, 120, 2373

Schlegel, E.M. et al. 2004, *ApJ*, 603, 644

Shapley, A., Fabbiano, G., & Eskridge, P.B. 2001, *ApJS*, 137, 139

Schlegel, E.M., Petre, R., Colbert, E.J.M., & Miller, S. 2000, *AJ*, 120, 2373

Smith, D.A. & Wilson, A.S. 2001, *ApJ*, 557, 180

Stocke, J.T. et al. 1983, *ApJ*, 273, 458

Summers, L.K., Stevens, I.R., Strickland, D.K., & Heckman, T.M. 2003, *MNRAS*, 342, 690

Summers, L.K., Stevens, I.R., Strickland, D.K., & Heckman, T.M. 2004, *MNRAS*, 351, 1

Sunyaev, R.A. & Titarchuk, L.G. 1980, *A&A*, 86, 121

Swartz, D.A., Ghosh, K.K., Tennant, A.F., & Wu, K. 2004, *ApJS*, 154, 519

Terashima, Y. & Wilson, A.S. 2004, *ApJ*, 601, 735

Tolstoy, E., Saha, A., Hoessel, J.G., & McQuade, K. 1995, *AJ*, 110, 1640

Tosi, M., Bellazzini, M., Aloisi, A., Gregg, L., Leitherer, C., & Montegriffo, P. 2001, *AJ*, 122, 1271

Tully, R.B. 1988, *Nearby Galaxies Catalog*. Cambridge Univ. Press, Cambridge

Voges, W. et al. 1999, *A&A*, 349, 389

Vogler, A. & Pietsch, W. 1996, *A&A*, 311, 35

Wang, D. et al. 2004, *ApJ*, 609, 113

Zdziarski, A. A. & Gierliński, M. 2004, *Progress of Theoretical Physics Supplement*, 155, 99

Zimmermann, H.U. & Aschenbach, B. 2003, *A&A*, 406, 969

Table 1. *XMM-Newton* Galaxy Observations

Galaxy	Type ^a	n_H ^b	distance ^c	ref	obs id ^d	duration (s)	comments
NGC247	SAB(s)d	1.54	3.09	...	0110990301	14536	-
NGC253	SAB(s)c;HII	1.40	3.73	...	0110900101, 0152020101	30711, 110591	Starburst
NGC300	SA(s)d	3.11	2.56	...	0112800101	43967	-
NGC625	SB(s)m? sp; HII	2.15	2.62	...	0085100101	26288	-
NGC1313	SB(s)d; HII	4.0	4.17	...	0106860101	41310	-
IC0342	SAB(rs)cd; HII	30.3	3.9	1	0093640901	11217	-
NGC1569	IBm	21.7	1.6	1	0112290801	15582	Starburst
NGC1705	SA0- pec; HII	3.9	5.1	2	0148650101	58926	Starburst
MRK 71	BCD; HII	3.9	3.4	3	0141150201	45919	galaxy pair
NGC2403	SAB(s)cd; HII	4.15	3.56	...	0150651201	11415	-
Holmberg II	Im	3.42	2.70	...	0112520701, 0112520901	13528, 6860	-
Holmberg I	IAB(s)m	3.49	3.6	4	0026340101	26280	-
M81	SA(s)ab;LINER	4.12	3.6	4	0111800101	127913	Hol IX also in field of view
M82	Io; HII	4.14	3.9	5	0112290201	29387	Starburst
Holmberg IX	Im	4.0	3.6	4	0112521001	10350	M81 also in field of view
Sextans A	IBm	3.85	1.4	6	0026340201	21618	-
IC 2574	SAB(s)m	2.29	3.6	7	0026340301	24263	bursting star-formation
NGC 4214	IAB(s)m; HII	1.49	2.7	...	0035940201	14744	-
NGC 4258	SAB(s)bc;LINER	1.2	7.2	...	0059140901, 0110920101	16146, 21895	-
NGC4395	SA(s)m;LINER	1.33	4	...	0112521901	15842	-
NGC4449	IBm; HII	1.39	3.08	...	0112521701	15522	-
NGC4490	SB(s)d	1.78	7.8	1	0112280201	17754	interacting with NGC4485
NGC4631	SB(s)d	1.28	7.5	1	0110900201	53850	-
NGC4736	(R)SA(r)ab;LINER	1.43	4.3	1	0094360601	23461	-
NGC4945	SB(s)cd; Sy2	15.9	3.1	...	0112310301	23062	-
NGC 5204	SA(s)m; HII	1.42	4.8	1	0142770101, 0142770301	19205, 16387	-
M51	Sc; Sy2	1.55	7.2	1	0112840201	20924	Galaxy pair
M83	SAB(s)c;HII	3.94	6.2	...	0110910201	30627	Starburst
NGC5253	Im pec;HII	3.77	3.2	1	0035940301	47216	Starburst
M101	SAB(rs)cd	1.17	7.4	8	0104260101	43019	-
NGC5408	IB(s)m; HII	5.73	4.8	9	0112290601	7757	-
Circinus	SA(s)b; Sy2	57.8	4	10	0111240101	110496	-

^afrom the NASA/IPAC Extragalactic Database (NED)

^bcolumn density in units of 10^{20} cm^{-2} , obtained from the web version of the nH FTOOL

^cdistance in Mpc (if no reference is given, obtained from the distance modulus given in LEDA)

^d*XMM-Newton* observation ids for the data examined in this survey

References. — (1)Tully 1988; (2) Tosi et al. 2001; (3) Tolstoy et al. 1995; (4) Freedman et al. 1994; (5) Sakai & Madore 1999; (6) Sakai, Madore, & Freedman 1996; (7)Shapley, Fabbiano, & Eskridge 2001; (8) Kelson 1996; (9) Karachentsev et al. 2002; (10) Freeman et al. 1977.

Table 2. *XMM-Newton* best fit: single component spectral fits

Source	Powerlaw			Bremsstrahlung				
	n_H^a	Γ	χ^2/dof	n_H^a	kT (keV)	χ^2/dof	F_X^b	L_X^c
NGC247 XMM2	$1.4^{+1.8}_{-1.1}$	$2.29^{+1.02}_{-0.57}$	47.7/54	< 0.65	$2.55^{+6.90}_{-1.61}$	48.8/54	0.33	0.38
NGC 253 XMM2 (obs 1)	$1.6^{+0.4}_{-0.3}$	$2.51^{+0.18}_{-0.17}$	69.1/74	$0.5^{+0.2}_{-0.3}$	$2.12^{+0.52}_{-0.37}$	74.7/74	0.52	0.87
NGC300 XMM4 ^d	2.5	9.07	90.6/45	0.27	0.14	117.6/45	-	-
NGC1313 XMM4	$1.86^{+0.5}_{-0.4}$	$1.8^{+0.07}_{-0.12}$	141.7/149	$1.2^{+0.3}_{-0.3}$	$6.62^{+2.3}_{-1.48}$	140.1/149	0.33	0.69
IC0342 XMM1	$5.8^{+0.6}_{-0.3}$	$1.68^{+0.08}_{-0.08}$	159.5/185	$4.9^{+0.5}_{-0.4}$	$10.5^{+3.3}_{-1.9}$	160/185	3.5	6.37
IC0342 XMM2	$23.9^{+4.0}_{-3.6}$	$1.85^{+0.22}_{-0.20}$	77.5/85	$21^{+3.0}_{-2.8}$	$8.5^{+5.0}_{-2.4}$	74.9/85	4.64	8.44
IC0342 XMM4	$5.3^{+1.4}_{-1.2}$	$2.02^{+0.20}_{-0.19}$	64/58	$4.2^{+0.99}_{-0.85}$	$4.44^{+1.68}_{-0.74}$	56.9/58	0.69	1.26
MRK71 XMM1	$0.47^{+0.30}_{-0.32}$	$1.69^{+0.11}_{-0.13}$	55.3/54	$0.04^{+0.26}_{-0.04}$	$7.98^{+4.90}_{-2.92}$	59/56	0.19	0.27
NGC2403 XMM4	$1.7^{+0.8}_{-0.7}$	$1.89^{+0.30}_{-0.25}$	62.3/71	$1.1^{+0.5}_{-0.3}$	$4.59^{+4.1}_{-1.5}$	62.3/71	0.31	0.48
HolmII XMM1 (obs 2)	$1.5^{+0.2}_{-0.2}$	$3.09^{+0.15}_{-0.12}$	266.7/252	$0.31^{+0.12}_{-0.15}$	$1.13^{+0.11}_{-0.11}$	309.4/252	3.5	3.1
Holm I XMM2	0.35 ^e	$2.13^{+0.16}_{-0.15}$	39.2/45	0.35 ^e	$2.0^{+0.57}_{-0.48}$	68.8/45	0.10	0.16
Holm I XMM3	0.35 ^e	$2.05^{+0.19}_{-0.18}$	34.4/32	0.35 ^e	$2.03^{+0.85}_{-0.56}$	42.1/32	0.12	0.19
IC2574 XMM1	$1.3^{+0.40}_{-0.30}$	$1.97^{+0.07}_{-0.10}$	120.9/103	$0.69^{+0.23}_{-0.25}$	$4.1^{+0.89}_{-0.67}$	107.5/103	0.35	0.47
IC2574 XMM2	$0.4^{+0.4}_{-0.3}$	$2.2^{+0.21}_{-0.09}$	45.7/51	0.229 ^e	$1.71^{+0.33}_{-0.27}$	65.4/52	0.22	0.34
IC2574 XMM3	$0.15^{+0.35}_{-0.14}$	$2.43^{+0.27}_{-0.18}$	40.3/49	0.229 ^e	$0.97^{+0.18}_{-0.14}$	76.5/49	0.22	0.34
NGC4214 XMM1	$1.1^{+0.52}_{-0.47}$	$1.87^{+0.26}_{-0.21}$	41.9/38	$0.54^{+0.41}_{-0.35}$	$4.86^{+4.52}_{-1.66}$	44.5/38	0.25	0.22
NGC4258 XMM2 (obs 2)	$6.71^{+2.6}_{-1.5}$	$2.49^{+0.44}_{-0.33}$	83.6/57	$4.8^{+0.9}_{-1.3}$	$2.61^{+1.22}_{-0.72}$	85.5/57	0.30	1.9
NGC4258 XMM3	$1.4^{+0.69}_{-0.64}$	$2.32^{+0.34}_{-0.24}$	38.9/37	$0.49^{+0.44}_{-0.38}$	$2.48^{+1.09}_{-0.74}$	41.3/37	0.20	1.2
...	3.8	1.82	4/11	2.7	7.14	5/11	0.077	0.48
NGC4258 XMM4	$0.68^{+0.24}_{-0.42}$	$1.97^{+0.22}_{-0.19}$	41.1/48	$0.06^{+0.31}_{-0.05}$	$4.07^{+1.6}_{-1.2}$	45.2/48	0.39	2.4
...	$1.9^{+0.78}_{-0.60}$	$2.24^{+0.29}_{-0.24}$	77.03/77	$0.9^{+0.6}_{-0.4}$	$2.82^{+1.2}_{-0.8}$	77.8/77	0.33	2.0
NGC4395 XMM2	$0.33^{+0.6}_{-0.3}$	$2.75^{+0.45}_{-0.33}$	38.6/36	0.133^e	$0.79^{+0.13}_{-0.13}$	52/37	0.15	0.28
NGC4395 XMM4	$0.3^{+0.6}_{-0.3}$	$2.08^{+0.39}_{-0.30}$	16/25	0.133^e	$1.97^{+0.99}_{-0.60}$	21.6/26	0.15	0.28
NGC4449 XMM2	$1.5^{+0.3}_{-0.3}$	$2.81^{+0.16}_{-0.14}$	103.5/112	$0.25^{+0.2}_{-0.2}$	$1.65^{+0.62}_{-0.21}$	112.1/112	0.29	0.33
NGC4490 XMM4	$10.2^{+2.3}_{-1.8}$	$2.09^{+0.23}_{-0.19}$	51.6/50	$8.3^{+1.3}_{-1.5}$	$4.75^{+1.82}_{-0.90}$	50.3/50	0.84	6.1
NGC4490 XMM5	$3.9^{+0.94}_{-0.81}$	$2.31^{+0.22}_{-0.20}$	60.1/65	$2.5^{+0.54}_{-0.59}$	$3.08^{+0.89}_{-0.62}$	61.6/65	0.41	2.98
NGC4631 XMM4 ^d	7.8	9.50	261.5/74	2.9	0.17	207.8/74	-	-
NGC4631 XMM5 ^f	1.3	1.03	641.8/153	1.3	199	659/153	-	-
NGC4945 XMM3	$3.3^{+1.3}_{-0.9}$	$1.82^{+0.12}_{-0.20}$	30.1/30	$2.5^{+0.83}_{-0.90}$	$6.07^{+4.50}_{-1.71}$	30.3/30	0.38	0.43
NGC5204 XMM2	$0.89^{+0.49}_{-0.53}$	$1.98^{+0.25}_{-0.20}$	42.37/42	$0.23^{+0.3}_{-0.22}$	$4.05^{+1.51}_{-0.95}$	42.2/42	0.15	0.41
...	$0.75^{+0.45}_{-0.45}$	$1.63^{+0.20}_{-0.17}$	41.4/47	$0.42^{+0.46}_{-0.38}$	$7.82^{+5.03}_{-2.70}$	39.4/47	0.25	0.69
M51 XMM3	$0.6^{+0.30}_{-0.40}$	$1.86^{+0.09}_{-0.15}$	63.2/72	$0.05^{+0.3}_{-0.02}$	$5.22^{+2.26}_{-1.41}$	69.2/72	0.18	1.1
M51 XMM4	$0.4^{+0.20}_{-0.30}$	$1.55^{+0.08}_{-0.13}$	34.8/37	$0.01^{+0.17}_{-0.13}$	$11.1^{+0.32}_{-0.25}$	34.8/37	0.16	0.99

^atotal column density in units of 10^{21} cm^{-2}

^bunabsorbed flux in the 0.3-10 keV band in units of $10^{-12} \text{ erg cm}^{-2} \text{ s}^{-1}$

^cunabsorbed luminosity in the 0.3-10 keV band, using the distances quoted in Table 1, in units of $10^{39} \text{ erg s}^{-1}$

^dsee appendix; super-soft X-ray source best fit by single-component blackbody

^eabsorbtion column density fixed to the galactic column density found in Table 1

^fsource is best fit by a combined power law and *vapc* model; see appendix

Table 3. *XMM-Newton* best fit: two-component blackbody and power law spectral fits

Source	n_H^a	kT (keV)	Γ	χ^2/dof	$\Delta\chi^2^b$	F_X^c	L_X^d
NGC247 XMM1	$4.1^{+1.9}_{-1.5}$	$0.12^{+0.03}_{-0.02}$	$4.18^{+1.79}_{-2.52}$	86.5/93	25.7	6.2	7.1
NGC253 XMM1	$2.7^{+0.4}_{-0.4}$	$0.80^{+0.12}_{-0.09}$	$1.74^{+0.17}_{-0.14}$	225.9/230	36.7	2.7	4.5
...	$7.3^{+1.1}_{-0.9}$	$1.14^{+0.07}_{-0.10}$	$2.54^{+0.27}_{-0.22}$	567/580	44.6	3.4	5.7
NGC253 XMM2 (obs 2)	$2.0^{+0.3}_{-0.2}$	$0.71^{+0.10}_{-0.10}$	$2.14^{+0.05}_{-0.08}$	460.3/498	47.1	1.6	2.7
NGC253 XMM3	$3.1^{+4.8}_{-0.5}$	$0.75^{+0.13}_{-0.10}$	$2.47^{+2.99}_{-0.41}$	68.5/82	23.4	0.60	1.0
...	$3.2^{+0.7}_{-0.5}$	$0.67^{+0.13}_{-0.09}$	$2.07^{+0.14}_{-0.20}$	347.4/407	34.4	0.80	1.3
NGC253 XMM4	$20^{+10.8}_{-7.6}$	$0.11^{+0.03}_{-0.03}$	$2.51^{+0.49}_{-0.30}$	66.7/57	6.9	15	25
...	$4.5^{+1.2}_{-1.9}$	$0.09^{+0.02}_{-0.01}$	$2.33^{+0.27}_{-0.22}$	309.3/291	12.1	1.4	2.2
NGC253 XMM5	$1.5^{+7.2}_{-1.5}$	$0.96^{+0.24}_{-0.32}$	$2.43^{+3.06}_{-1.36}$	26.5/23	5.3	0.26	0.43
...	$4.6^{+1.1}_{-0.7}$	$0.16^{+0.02}_{-0.03}$	$1.95^{+0.14}_{-0.11}$	223.7/296	60.1	1.4	2.2
NGC253 XMM6	$6.3^{+2.1}_{-1.1}$	$0.12^{+0.02}_{-0.02}$	$2.26^{+0.18}_{-0.12}$	417.9/407	17.1	1.9	3.1
NGC253 XMM7	$6.3^{+0.9}_{-1.1}$	$0.69^{+0.11}_{-0.12}$	$2.40^{+0.41}_{-0.17}$	335.8/339	21.2	1.1	1.8
NGC300 XMM1	$1.7^{+0.20}_{-0.30}$	$0.98^{+0.14}_{-0.10}$	$3.41^{+0.06}_{-0.26}$	443.7/420	26.1	1.3	1.0
NGC300 XMM2	$3.8^{+1.4}_{-1.4}$	$0.09^{+0.01}_{-0.01}$	$2.87^{+0.34}_{-0.38}$	102.6/97	31.34	1.1	0.86
NGC300 XMM3	$4.4^{+1.0}_{-0.8}$	$0.04^{+0.25}_{-0.01}$	$1.98^{+0.1}_{-0.1}$	87.7/79	14.2	1.2	0.93
NGC300 XMM6	$2.3^{+2.6}_{-1.3}$	$0.84^{+0.25}_{-0.19}$	$4.9^{+1.97}_{-0.7}$	34.6/35	13	0.27	0.20
NGC1313 XMM1	$3.0^{+1.2}_{-0.9}$	$0.13^{+0.03}_{-0.02}$	$1.75^{+0.14}_{-0.11}$	194.1/201	35.4	0.64	1.3
NGC1313 XMM2	$3.1^{+0.4}_{-0.3}$	$0.16^{+0.04}_{-0.02}$	$2.27^{+0.10}_{-0.14}$	425.2/419	38.9	2.0	4.2
NGC1313 XMM3	$6.2^{+0.8}_{-0.6}$	$0.11^{+0.01}_{-0.01}$	$2.76^{+0.10}_{-0.11}$	441.7/424	336.6	10	22
IC0342 XMM3	$9.7^{+1.8}_{-2.1}$	$0.09^{+0.02}_{-0.01}$	$2.69^{+0.16}_{-0.23}$	129.5/107	56.3	31	56.4
NGC1705 XMM1	$0.29^{+0.39}_{-0.27}$	$1.01^{+0.41}_{-0.29}$	$2.31^{+0.89}_{-0.48}$	53/85	8.9	0.10	0.44
NGC1705 XMM3	< 1.44	$1.07^{+0.20}_{-0.15}$	$2.23^{+0.70}_{-0.56}$	69.8/65	11.1	0.15	0.48
NGC2403 XMM1	$2.3^{+1.2}_{-1.1}$	$0.66^{+0.16}_{-0.18}$	$2.18^{+0.41}_{-0.59}$	81.4/79	10.8	1.99	3.1
NGC2403 XMM2	$1.8^{+0.8}_{-0.6}$	$0.62^{+0.16}_{-0.11}$	$1.95^{+0.26}_{-0.42}$	163.1/151	16.4	1.0	1.6
NGC2403 XMM3	$1.7^{+1.1}_{-0.8}$	$0.74^{+0.23}_{-0.21}$	$2.15^{+0.66}_{-0.40}$	84.2/105	8.4	0.64	1.1
Holm II XMM1(obs 1)	$1.6^{+0.1}_{-0.2}$	$0.14^{+0.02}_{-0.01}$	$2.35^{+0.05}_{-0.11}$	997.5/976	136.7	12	10
M81 XMM1	$3.3^{+0.17}_{-0.08}$	$0.90^{+0.03}_{-0.03}$	$2.52^{+0.03}_{-0.04}$	1273.7/1243	533.1	4.5	7.0
...	$3.5^{+0.4}_{-0.6}$	$1.13^{+0.13}_{-0.14}$	$2.34^{+0.29}_{-0.36}$	203.5/204	21.4	4.8	7.4
M81 XMM2	$7.4^{+0.5}_{-0.7}$	$0.1^{+0.004}_{-0.004}$	$2.87^{+0.16}_{-0.17}$	833.9/616	524.3	13	22
M81 XMM4	$1.1^{+1.6}_{-1.0}$	$2.51^{+1.11}_{-0.73}$	$2.31^{+1.22}_{-1.05}$	48.9/50	28.2	0.43	0.70
M81 XMM5	$0.15^{+0.69}_{-0.13}$	$0.62^{+0.19}_{-0.11}$	$1.26^{+0.22}_{-0.20}$	89/80	8.5	0.38	0.59
Holm IX XMM1	$2.1^{+0.2}_{-0.2}$	$0.17^{+0.02}_{-0.02}$	$1.72^{+0.04}_{-0.03}$	866.6/878	134.3	10	16
NGC4258 XMM1	$0.38^{+0.96}_{-0.3}$	$0.54^{+0.17}_{-0.08}$	$1.51^{+0.4}_{-0.4}$	91.1/76	10.3	0.34	2.1
NGC4258 XMM2 (obs 1)	$1.9^{+2.4}_{-0.4}$	$0.78^{+0.12}_{-0.13}$	$2.02^{+0.65}_{-1.8}$	73.4/61	24.1	0.31	1.9
NGC4395 XMM1	$2.0^{+0.08}_{-0.07}$	$0.14^{+0.02}_{-0.02}$	$3.44^{+0.54}_{-0.56}$	168.2/154	26.9	1.4	2.7
NGC4449 XMM1	$8.7^{+4.8}_{-2.1}$	$0.19^{+0.13}_{-0.07}$	$2.21^{+0.33}_{-0.29}$	111.2/116	4.3	1.56	1.8
NGC4449 XMM3	$3.5^{+1.3}_{-0.9}$	$0.15^{+0.03}_{-0.03}$	$2.52^{+0.36}_{-0.39}$	119.9/87	34.1	1.1	1.3
NGC4490 XMM1	$5.8^{+2.96}_{-2.96}$	$0.77^{+0.08}_{-0.095}$	$2.89^{+1.77}_{-0.61}$	66.5/63	35	0.88	6.4
NGC4631 XMM1	$3^{+0.9}_{-0.5}$	$0.12^{+0.03}_{-0.02}$	$2.12^{+0.63}_{-0.02}$	371.3/345	12.1	0.96	6.5
NGC4631 XMM2	$2.3^{+1.4}_{-0.3}$	$0.18^{+0.05}_{-0.06}$	$1.80^{+0.12}_{-0.09}$	107.4/97	12.1	0.25	1.7
NGC4631 XMM3	$1.1^{+1.1}_{-0.8}$	$1.01^{+0.12}_{-0.1}$	$2.45^{+1}_{-0.62}$	127.1/96	18.9	0.15	1.0
NGC4945 XMM1	$3.5^{+2.1}_{-1.1}$	$0.77^{+0.27}_{-0.10}$	$1.60^{+0.40}_{-0.31}$	96.1/120	20	0.59	0.68
NGC4945 XMM2	$3.2^{+1.1}_{-0.7}$	$1.15^{+0.28}_{-0.33}$	$1.80^{+0.20}_{-0.30}$	105.8/113	8.7	0.66	0.76
NGC4945 XMM4	$4.0^{+2.0}_{-1.1}$	$0.61^{+0.10}_{-0.10}$	$2.82^{+1.06}_{-0.58}$	58.4/60	17.1	0.38	0.44
NGC5204 XMM1	$0.66^{+0.35}_{-0.08}$	$0.16^{+0.02}_{-0.03}$	$1.92^{+0.12}_{-0.06}$	543.0/559	49.1	1.98	5.6
...	$1.1^{+0.08}_{-0.14}$	$0.16^{+0.02}_{-0.02}$	$2.03^{+0.12}_{-0.12}$	461.4/496	71.6	2.92	8.0

Table 3—Continued

Source	n_H^a	kT (keV)	Γ	χ^2/dof	$\Delta\chi^2^b$	F_X^c	L_X^d
M51 XMM1	$0.95^{+1.10}_{-0.18}$	$0.16^{+0.03}_{-0.05}$	$2.15^{+0.42}_{-0.17}$	97/80	13.4	0.31	1.9
M51 XMM5	$10.4^{+1.7}_{-3.7}$	$0.078^{+0.01}_{-0.01}$	$2.26^{+0.26}_{-0.25}$	59.8/70	196.2	220	1900
M83 XMM4	$1.77^{+3.9}_{-1.77}$	$0.54^{+0.18}_{-0.09}$	$1.61^{+0.96}_{-0.31}$	84.8/89	6.6	0.2	0.92
M101 XMM1	$0.22^{+0.12}_{-0.15}$	$0.21^{+0.03}_{-0.04}$	$1.42^{+0.14}_{-0.05}$	249.9/231	53.1	0.45	2.9
M101 XMM2	$1.6^{+0.46}_{-0.21}$	$0.76^{+0.14}_{-0.10}$	$1.88^{+0.25}_{-0.11}$	251.6/261	37.2	0.7	4.6
NGC5408 XMM1	$0.9^{+0.21}_{-0.16}$	$0.14^{+0.01}_{-0.01}$	$2.71^{+0.16}_{-0.20}$	316.4/337	80.4	3.97	10.9
CIRCINUS XMM1	$10.1^{+1.2}_{-1.2}$	$0.10^{+0.01}_{-0.01}$	$2.30^{+0.08}_{-0.08}$	749.4/861	13.5	12	23
CIRCINUS XMM2	$11.2^{+2.4}_{-1.7}$	$0.53^{+0.03}_{-0.03}$	$4.71^{+0.94}_{-0.49}$	438.5/430	79.4	5.6	10.7
CIRCINUS XMM3	$13.5^{+5.5}_{-5.6}$	$0.67^{+0.10}_{-0.08}$	$5.77^{+2.24}_{-2.3}$	269.3/260	15.9	7.6	14.5

^atotal column density in units of 10^{21} cm^{-2}

^bimprovement in χ^2 over the single-component power law model

^cunabsorbed flux in the 0.3-10 keV band in units of $10^{-12} \text{ erg cm}^{-2} \text{ s}^{-1}$

^dunabsorbed luminosity in the 0.3-10 keV band, using the distances quoted in Table 1, in units of $10^{39} \text{ erg s}^{-1}$

Table 4. *XMM-Newton* two-component blackbody and power law spectral fits for sources with large uncertainty

Source	n_H^a	kT (keV)	Γ	χ^2/dof	$\Delta\chi^2^b$	F_X^c	L_X^d
NGC300 XMM5	$0.41^{+0.60}_{-0.30}$	$1.06^{+0.37}_{-0.20}$	$2.78^{+0.61}_{-0.65}$	46.6/53	7.6	0.17	0.13
NGC1705 XMM2	$0.96^{+0.97}_{-0.32}$	$0.23^{+0.10}_{-0.11}$	$1.60^{+1.97}_{-0.27}$	85.5/74	6.5	0.09	0.27
Holm I XMM1	$0.4^{+0.5}_{-0.3}$	$1.97^{+0.66}_{-0.89}$	$2.46^{+0.44}_{-0.40}$	97.4/93	5.4	0.6	0.93
M81 XMM3	$3.7^{+2.4}_{-2.1}$	$0.11^{+0.05}_{-0.02}$	$1.69^{+0.37}_{-0.33}$	77.1/78	4.25	0.53	0.82
Sextans A XMM1	$0.4^{+0.7}_{-0.1}$	$1.05^{+2.3}_{-0.07}$	$2.6^{+0.2}_{-0.2}$	269.1/271	2.3	0.60	0.14
NGC4214 XMM2	$1.8^{+1.9}_{-0.6}$	$0.81^{+0.56}_{-0.20}$	$3.95^{+1.81}_{-1.05}$	46.4/44	4.5	0.4	0.35
NGC4395 XMM3	$0.5^{+0.9}_{-0.3}$	$1.10^{+0.67}_{-0.18}$	$2.66^{+1.05}_{-0.77}$	52/56	3.9	0.29	0.56
NGC4490 XMM2	$4.4^{+1.9}_{-1.9}$	$0.60^{+0.20}_{-0.12}$	$2.13^{+0.50}_{-0.70}$	42.4/54	7.1	0.65	4.7
NGC4490 XMM3	$13^{+9.6}_{-2.5}$	$0.09^{+0.02}_{-0.02}$	$3.21^{+0.52}_{-0.17}$	72.1/78	4.6	12	87.4
NGC4736 XMM1	$6.3^{+3.0}_{-3.7}$	$0.08^{+0.03}_{-0.02}$	$2.41^{+0.34}_{-0.27}$	54.9/51	7.9	8.1	17.9
M51 XMM2	$1.3^{+0.6}_{-0.5}$	$0.26^{+0.07}_{-0.08}$	$1.80^{+0.61}_{-0.92}$	70.7/68	4.5	0.36	3.0
M51 XMM6	$8.2^{+3.5}_{-5.6}$	$0.08^{+0.05}_{-0.02}$	$3.0^{+0.37}_{-0.43}$	36.9/41	4.07	5.6	35
M51 XMM7	$2.8^{+3.4}_{-2.1}$	$0.10^{+0.03}_{-0.03}$	$1.97^{+0.43}_{-0.30}$	31.7/29	6.1	0.26	1.6
M83 XMM1	$1.6^{+0.48}_{-0.45}$	$0.74^{+0.23}_{-0.26}$	$2.58^{+0.60}_{-0.24}$	177.7/209	4.7	0.63	2.5
M101 XMM3	$1.98^{+1.0}_{-0.61}$	$0.63^{+0.22}_{-0.20}$	$2.93^{+0.15}_{-0.26}$	145.5/131	3.4	0.56	3.7
M101 XMM4	$1.8^{+0.17}_{-0.15}$	$0.54^{+0.11}_{-0.07}$	$2.22^{+0.12}_{-0.08}$	158.2/138	7.5	0.34	2.2
M101 XMM5	$1.3^{+1.2}_{-0.2}$	$0.18^{+0.05}_{-0.06}$	$1.95^{+0.3}_{-0.22}$	45.1/44	2.8	0.13	0.85

^atotal column density in units of 10^{21} cm^{-2}

^bimprovement in χ^2 over the single-component power law model

^cunabsorbed flux in the 0.3-10 keV band in units of $10^{-12} \text{ erg cm}^{-2} \text{ s}^{-1}$

^dunabsorbed luminosity in the 0.3-10 keV band, using the distances quoted in Table 1, in units of $10^{39} \text{ erg s}^{-1}$

Table 5. Bolometric Luminosities of ULX sources

Source	$L_{cutoff\,fp}^a$	L_{bol}^b	M_{Edd}^c	class ^d
NGC247 XMM1	13.4258	7.07734	54	HS ULX
NGC253 XMM1	9.31469	2.44574	19	HS ULX
NGC253 XMM2	4.3701	2.15292	17	HS ULX
NGC253 XMM6	5.05828	3.92514	30	HS ULX
NGC1313 XMM3	37.0364	27.9692	215	HS ULX
NGC1313 XMM4	1.50345	...	116	LS IMBH cand.
IC0342 XMM1	14.1215	...	1086	LS ULX
IC0342 XMM2	19.8129	...	1524	LS ULX
IC0342 XMM3	114.015	95.4068	734	HS ULX
MRK71 XMM1	0.2993	...	23	LS IMBH cand.
NGC2403 XMM1	4.1497	2.14873	17	HS ULX
NGC2403 XMM4	0.57068	...	44	LS IMBH cand.
Holmberg II XMM1	0.88906	...	68	LS IMBH cand.
...	16.8335	11.4543	88	HS ULX
Holmberg I XMM2	10.5158	...	809	LS ULX
M81 XMM1	15.7004	3.17932	24	HS ULX
Holmberg IX XMM1	31.0582	28.1445	216	HS ULX
NGC4214 XMM1	0.26699	...	21	LS IMBH cand.
NGC4258 XMM3	0.46503	...	36	LS IMBH cand.
NGC4395 XMM1	9.04609	2.94683	23	HS ULX
NGC4449 XMM2	2.48586	...	191	LS IMBH cand.
NGC4490 XMM1	16.8513	3.21972	25	HS ULX
NGC4490 XMM2	7.36612	4.51554	35	HS ULX
NGC4490 XMM3	240.653	176.04	1354	HS ULX
NGC4490 XMM4	1.66829	...	128	LS IMBH cand.
NGC4490 XMM5	12.7136	...	978	LS ULX
NGC4631 XMM1	10.6527	8.59661	66	HS ULX
NGC4736 XMM1	31.6561	27.3664	211	HS ULX
NGC4945 XMM3	0.44985	...	35	LS IMBH cand.
NGC5204 XMM1	22.4756	2.20492	17	HS ULX
NGC5204 XMM2	5.57769	...	429	LS ULX
M51 XMM2	4.25898	3.57502	28	HS ULX
M51 XMM3	2.10133	...	162	LS IMBH cand.
M51 XMM4	2.56064	...	197	LS IMBH cand.
M51 XMM6	46.7642	39.5189	304	HS ULX
M101 XMM1	8.04916	7.68224	59	HS ULX
M101 XMM2	7.54268	4.96709	38	HS ULX
M101 XMM3	10.9792	1.03659	8	HS ULX
NGC5408 XMM1	20.9211	11.5369	89	HS ULX
Circinus XMM1	70.3579	56.1033	432	HS ULX
Circinus XMM2	208.746	0.69929	5	HS ULX
Circinus XMM3	771.157	0.212957	2	HS ULX

^aestimation of the bolometric luminosity, determined with an exponential cut-off in the power law at high energy (see text)

^bbolometric luminosity estimate for high-state ULXs where the power law is cut at twice kT_{in} (see text); units for both luminosity measurements in 10^{39} erg s $^{-1}$

^cmass computed for objects radiating at $0.1 \times L_{Edd}$ (low-state objects) or L_{Edd} (high-state objects; using L_{bol}), in units of M_{\odot}

^dclassification based on the criteria set forward in the text: high-state ULX (HS ULX), low-state ULX (LS ULX), and low-state IMBH candidate (low-state object with $10^{38} \text{ erg s}^{-1} < L_{bol} < 3 \times 10^{39} \text{ erg s}^{-1}$)

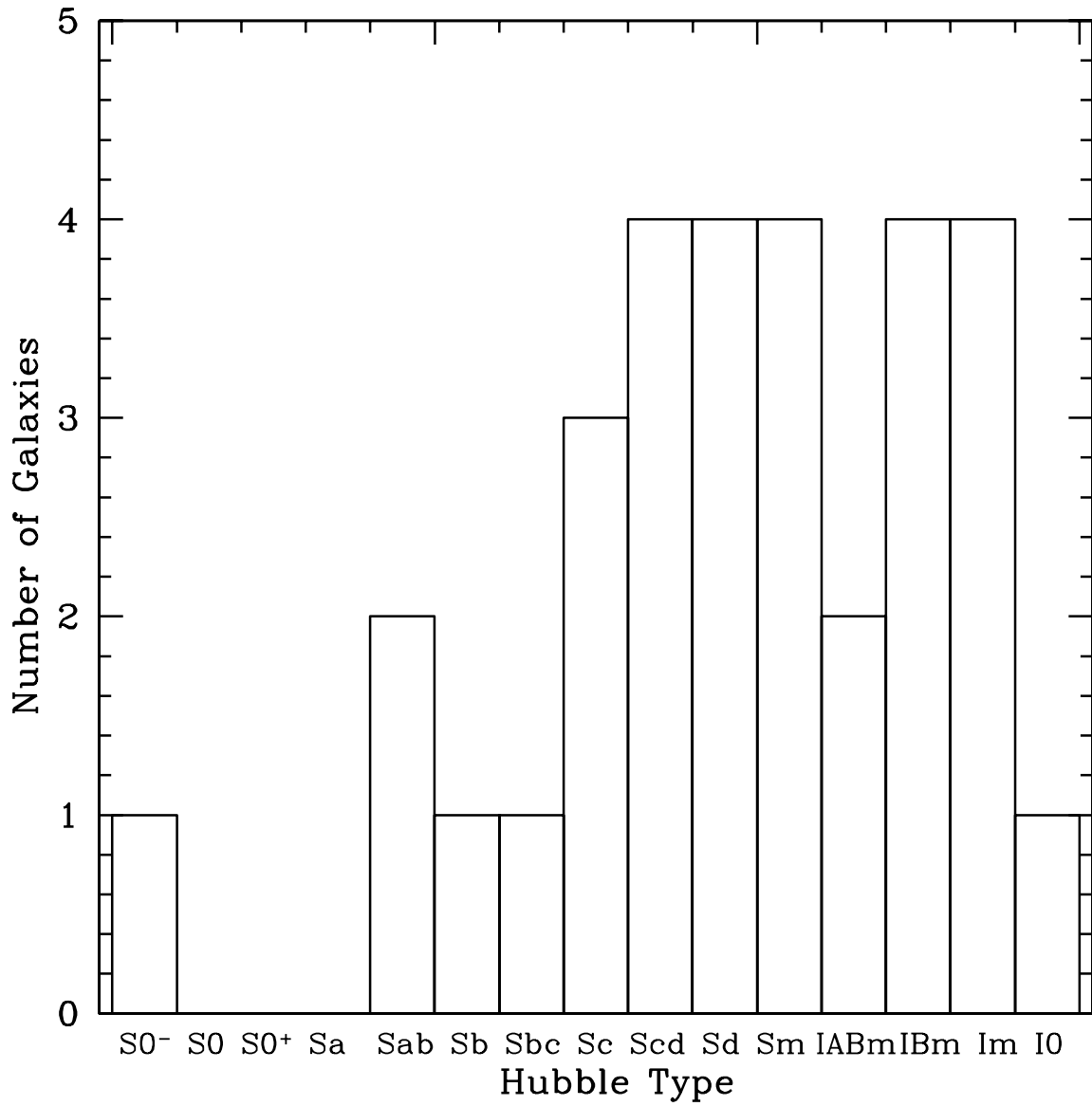


Fig. 1.— Distribution of galaxies by Hubble type among our archival *XMM-Newton* sample of nearby (< 8 Mpc) galaxies. Our sample consists solely of spirals and irregulars.

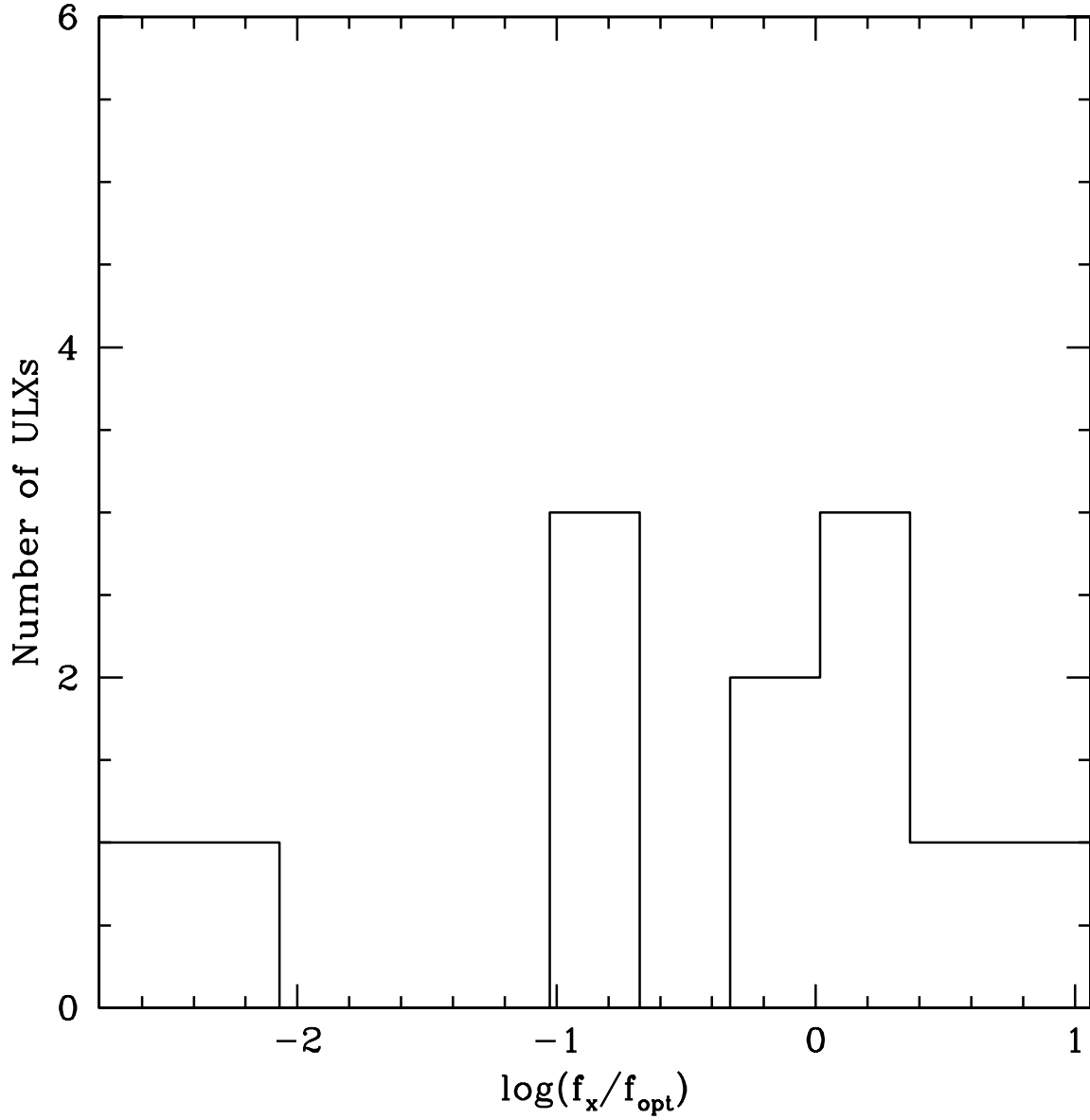


Fig. 2.— The distribution of f_x/f_{opt} for the brightest possible optical point source within the *XMM-Newton* error circle. We define f_x as the unabsorbed X-ray flux in the 0.3–10 keV range and f_{opt} as the optical flux obtained from the U filter of *XMM*'s OM (as described in text). These ratios do not represent the actual f_x/f_{opt} of the sources but are an estimate of the minimum possible value. A majority of the sources had no optical point source within the X-ray contour and thus have ratios of f_x/f_{opt} far higher than those indicated in the plot.

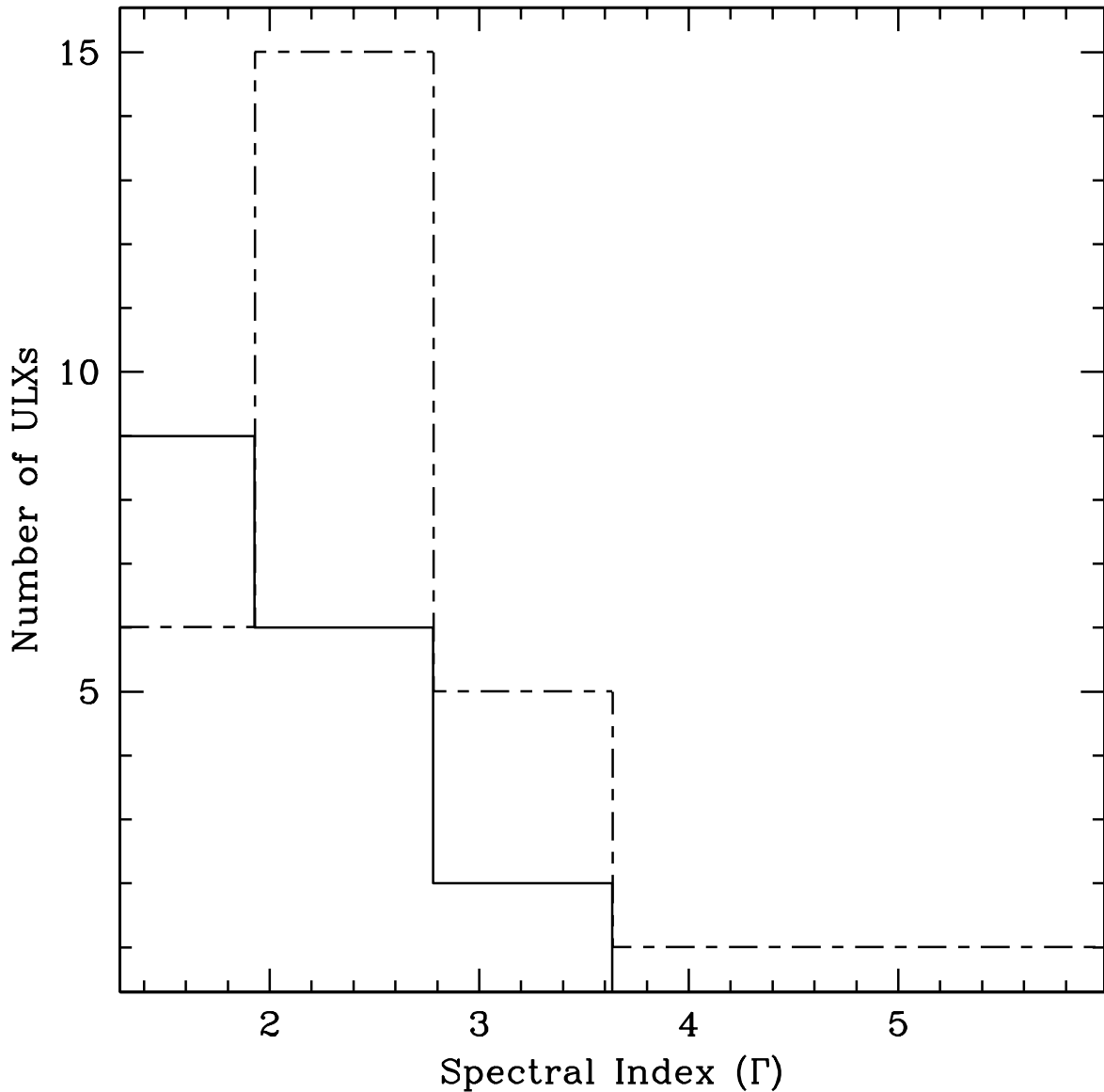


Fig. 3.— Distribution of the spectral indices (Γ) for low-state (solid) and high-state (dashed) objects. For Galactic low-state objects, typically $\Gamma \approx 2.0$, similar to our sample, while the high-state objects have a steeper Γ (McClintock & Remillard 2004).

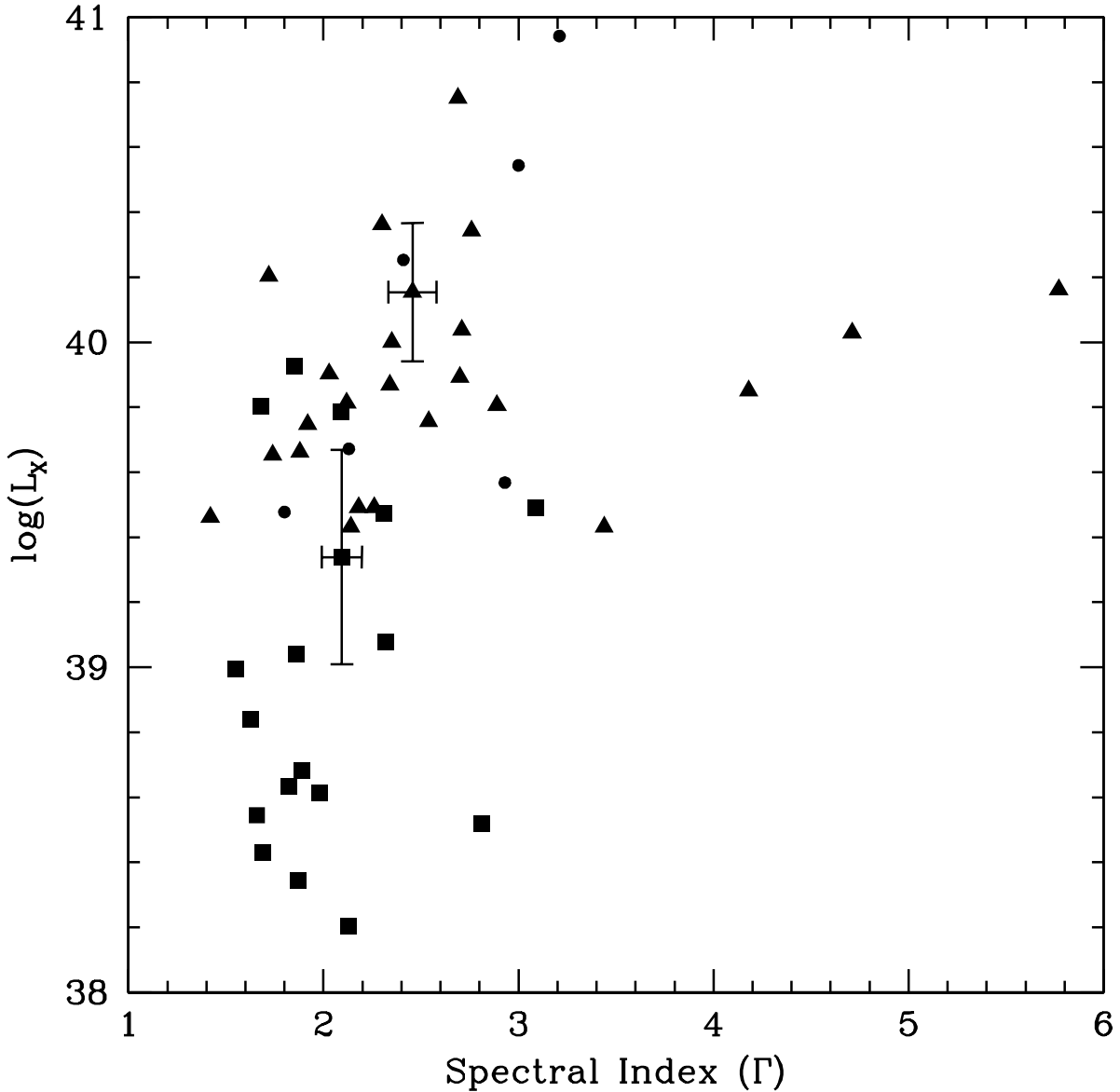


Fig. 4.— Relationship of luminosity vs. spectral index for low-state (rectangle) and high-state (triangle) objects. Sources represented by a circle are those where the $\Delta\chi^2$ value between the two-component and power law fits was very small. As expected from observations of Galactic stellar-mass black hole systems (McClintock & Remillard 2004), the classified low-state ULXs in our sample have, on average, lower X-ray luminosities than the corresponding high-state ULXs. We plot the mean values for both high-state and low-state objects with errorbars indicating the root mean square deviation. The outlying objects with spectral indices greater than 3.5 were not included in the mean or deviation calculations.

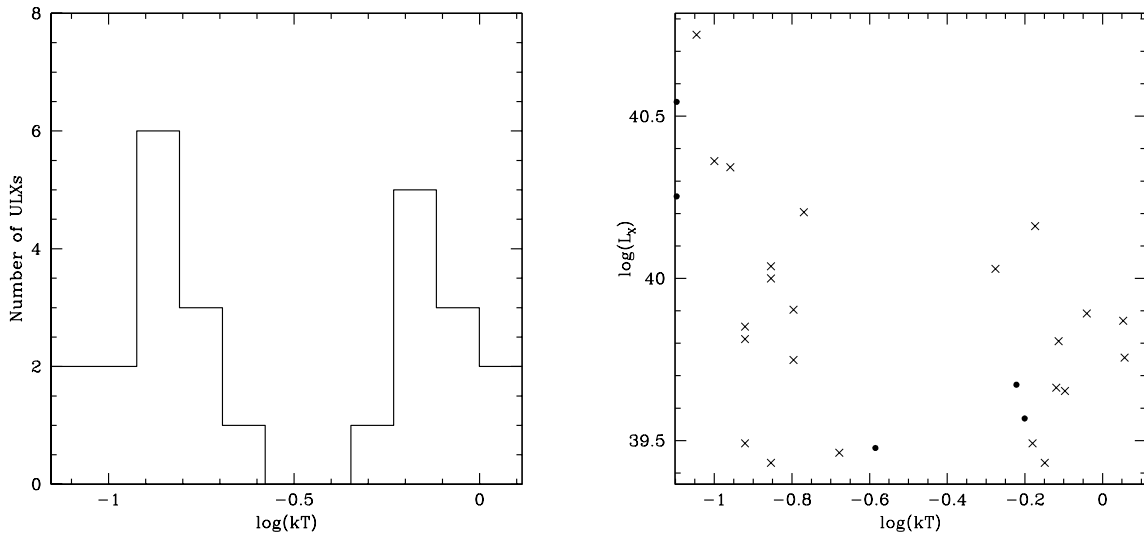


Fig. 5.— (left) Distribution of the blackbody temperature for high-state objects. (right) Relationship of blackbody temperature vs. luminosity (in the 0.3-10 keV band) for high-state objects. We see two peaks arise in the distribution, one centered around $kT \approx 0.1$ and another at $kT \approx 1$. The peak with a low disk temperature also corresponds to the highest luminosities, suggesting that these may be high-state IMBHs. The sources with higher disk temperature also have lower luminosities. The spectra of these sources were also well fit by an inverse Comptonization model (a model successfully used to fit some of the Galactic black hole X-ray binaries in the very high state).

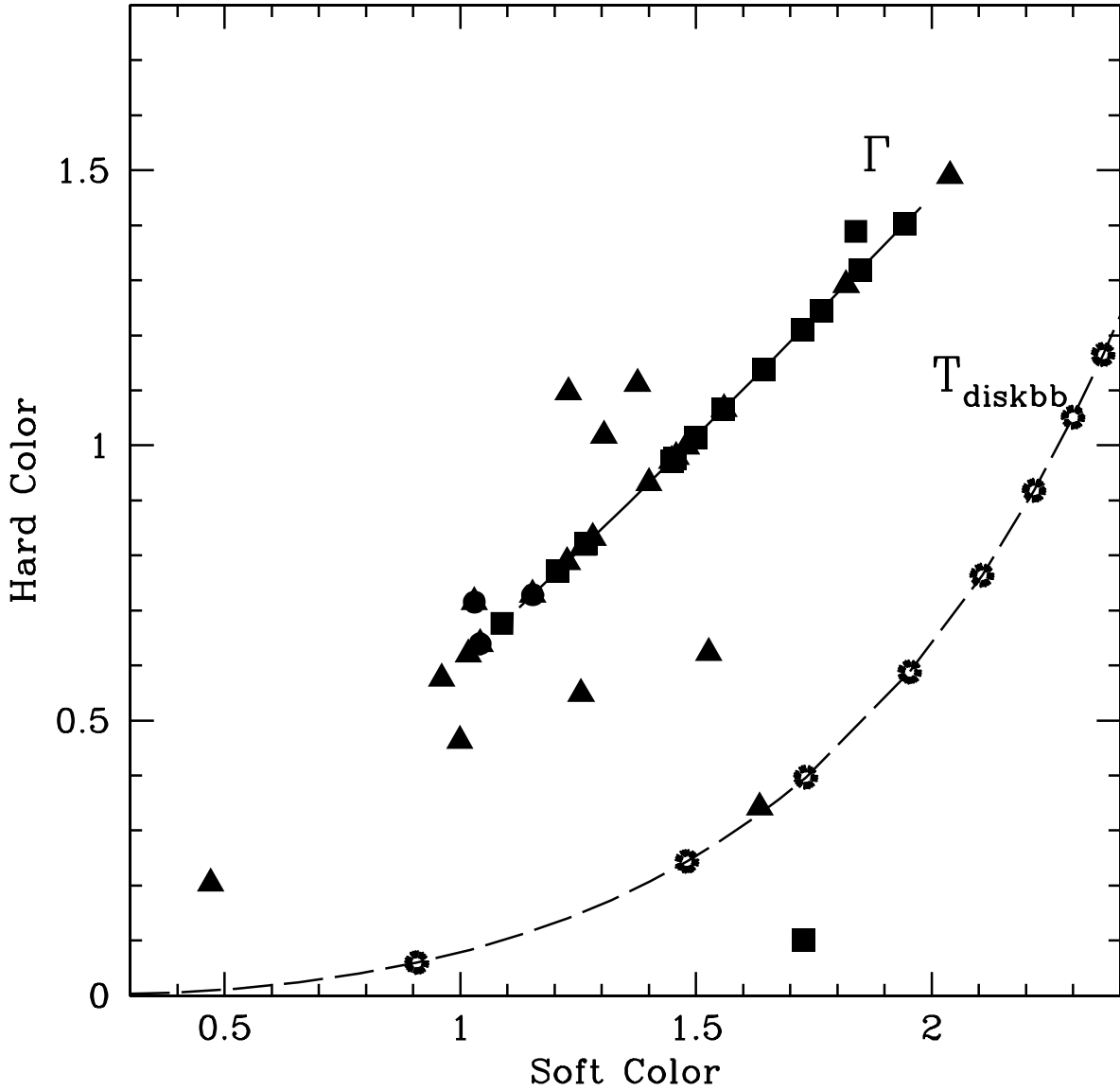


Fig. 6.— Color-Color Diagram plotting soft vs. hard colors, as outlined in Done & Gierlinski (2003), for low-state (rectangle) and high-state (triangle) ULXs. The filled circles represent the sources with low $\Delta\chi^2$ values between the two-component and power law models. A large number of our sources lie in the same range of this graph as the black hole sources examined by Done & Gierlinski (2003) (near the power law distribution, indicated by the solid line). The dashed line represents the color-color plot for a multi-colored disk model with different disk temperatures. The sources approaching this line were those well-fit by the Comptonization model. Done & Gierlinski (2003) had no black hole sources in this region, but atolls and Z-sources, which were also well-fit by Comptonization models.

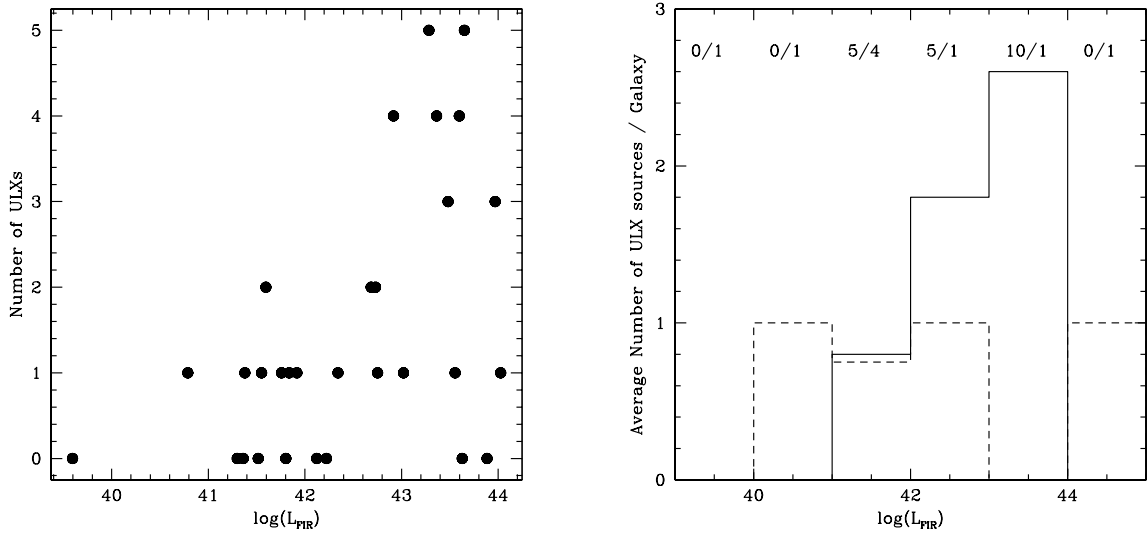


Fig. 7.— (left) Relationship of the far-infrared luminosity, as an indicator of star formation rate, vs. the number of ULXs for each galaxy. If ULXs are associated with star formation, we naively expect that the higher the FIR luminosity the more ULXs the galaxy will host. (right) The distribution of average number of ULXs / L_{FIR} bin for spirals (solid line) follows this expectation. The distribution of irregulars (dashed line) is not so easily interpreted. The numbers at the top indicate the number of spirals/irregulars in each of the luminosity bins. More irregulars would need to be included in this survey for meaningful statistics on this group.

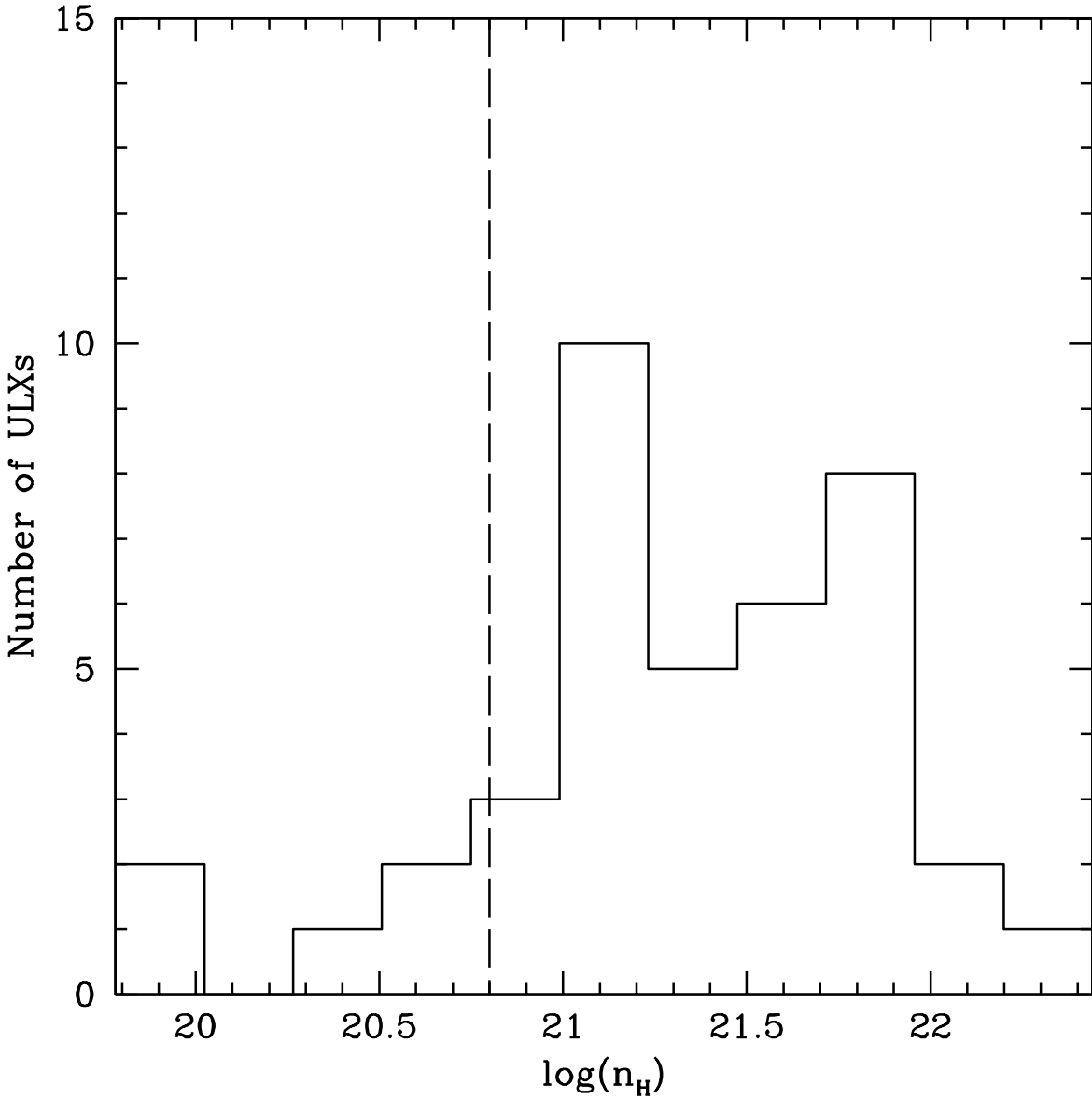


Fig. 8.— Distribution of the hydrogen column densities of ULX sources. The n_H values were obtained through spectral fits using the *wabs* model in *XSPEC*. Galactic column densities towards the host galaxy were subtracted from the spectral fit values. A majority of our ULX sources have high column densities ($> 10^{21} \text{ cm}^{-2}$), suggesting that some of this absorption originates with the local ULX environment. Bins to the left of the dashed line represent sources with column densities very close to the Galactic value and thus a simple subtraction is not statistically representative of the true value.

A. Spectral Simulations

A.1. Two-component Model

In order to determine the number of counts required to distinguish whether a blackbody component is statistically significant for the sources fit with a two-component model, we simulated spectra based on that of some of the brightest sources. We chose to simulate spectra of bright two-component spectra exhibiting three different cases: (1) the flux from the blackbody dominates over the power law component at 2 kT , (2) an intermediary case, and (3) the flux from the power law dominates over the blackbody component at 2 kT . Such simulations would allow us to determine the uncertainty in our claims of a combined fit being a better descriptor of the data. This is necessary because there is no a priori model which predicts the relative intensities of the two components and, as we know from studies of Galactic black holes, these components show a wide variety of relative intensities. To this end, we simulated spectra using the best-fit absorbed blackbody and power law model with the *fakeit* command in XSPEC. We chose (1) NGC 247 XMM1, (2) NGC 5408 XMM1, and (3) Holmberg II XMM1 as our seed observations. These objects all have very high signal-to-noise and thus the fits are robust. The respective ratios of powerlaw flux to blackbody flux contributions at 2 kT are: (1) $<< 1.0$, (2) 1.77, and (3) 3.52. All of these sources have comparable blackbody temperatures indicative of our high-state ULX candidates (roughly $\text{kT} \approx 0.15$).

We simulated 500 spectra each, using the two-component model, for each of 2000 counts, 1000 counts, 400 counts, and 200 counts for the PN. Each simulated spectrum, based on the best-fit blackbody and power law model, was fit with an absorbed blackbody and powerlaw model as well as an absorbed pure-powerlaw model. We placed the constraint that the blackbody temperature must lie within the range of $0.07 - 4.0\text{ keV}$ (the range at which it would be detectable in the *XMM-Newton* bandpass). We allowed the power law index to vary over the range $0 - 4$ for the power law component of the combined blackbody and power law model. However, we placed a constraint that the power law component must lie within the range $\Gamma = 1.5 - 2.0$ for the simple power law model to be consistent with our fits to the sources we claim are best fit by simple power laws. This constraint ensures that the spectral index would exhibit that of our classified “low-state” objects.

When analysing and classifying our real spectra, we declared a detection of the thermal disk component if the addition of this component (to a baseline powerlaw model) led to an improvement of the goodness of fit parameter by at least $\Delta\chi^2 = 8$. We can use the above simulations to address the detectability of a thermal disk component using this $\Delta\chi^2$ threshold as a function of the relative strength of the thermal component and the number of counts in the spectrum. For each simulation, we fit the spectrum with both a single absorbed power-law and a 2-component powerlaw and thermal disk model and compute the quantity $\Delta\chi^2 = \chi^2_{\text{pow}} - \chi^2_{\text{pow+disk}}$. In Fig. A1, we plot the distribution of $\Delta\chi^2$ from our 500 simulations for the weak and strong blackbody component for spectra with 400 counts and 2000 counts. It is clear that we cannot detect a weak thermal component in a 400 count spectrum — the vast majority of the simulations ($\approx 82\%$) result in $\Delta\chi^2 < 8$. However, even a weak thermal component is easily detected in a 2000 count spectrum (not a single simulation

gave $\Delta\chi^2 < 8$). The strong blackbody case is detectable with high significance even in a 400 count spectrum ($< 1\%$ of the simulations resulted in $\Delta\chi^2 > 8$).

When we increase the upper limit of the range of the spectral index in *XSPEC* for the power law model to $\Gamma = 3.0$, our confidence levels decrease. For a weak thermal component with 400 counts, all of the simulations result in $\Delta\chi^2 < 8$. At 2000 counts, only $\approx 30\%$ of the simulations for a weak thermal component have $\Delta\chi^2 < 8$. For a strong thermal component, 20% of the simulations yield $\Delta\chi^2 < 8$ for 400 counts while, as was the case for $\Gamma = 2.0$, none of the simulations gave $\Delta\chi^2 < 8$ for 2000 counts.

Thus allowing the Γ to “float freely” or remain unconstrained further decreases the confidence levels. When the Γ parameter is allowed to float the spectra are fit with higher Γ values in order to compensate for the missing blackbody component. When the upper limit was instituted at 2.0 or 3.0, we found that all 500 simulated spectra were fit with a $\Gamma = 2.0$ or 3.0, respectively, for the simple power law model. This same affect is not seen in the Γ of the two-component model, where the value ranges between 1.4 and 4.0 with a peak in the distribution near that of the original model used to simulate the spectra. Thus, higher power law indices (> 3.0) can indicate the necessity of an added blackbody component. Since there are no Galactic black holes whose broad band spectra are well fit by steep power laws it seems that restricting the allowed power law indices is more consistent with the nature of Galactic black holes. In fitting our sources with the three “standard” models, we allowed the Γ to float, thus the problem of a missing blackbody component being compensated for by a steep power law should not have factored into our classification criteria.

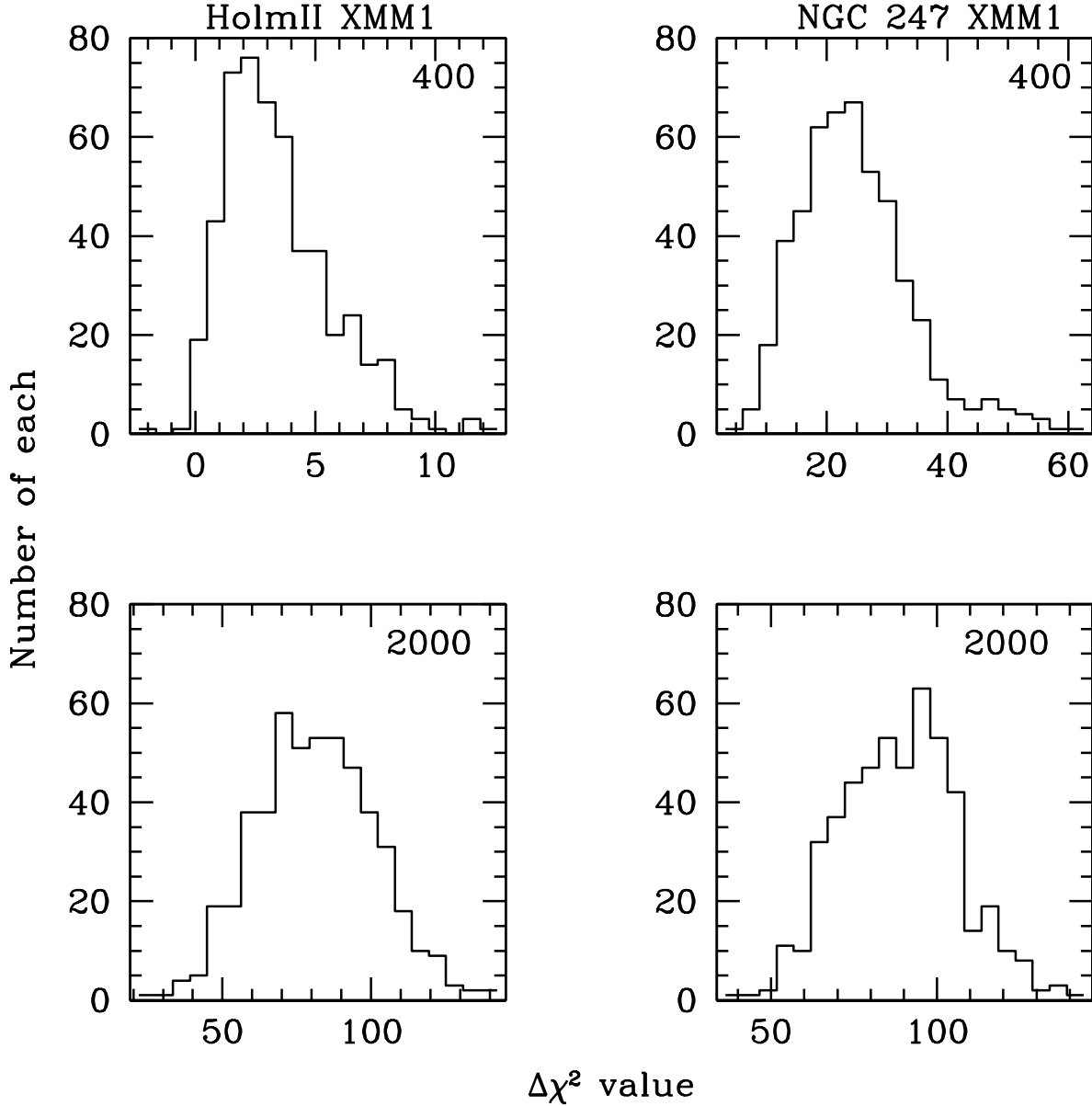


Fig. A1.— Distribution of $\Delta\chi^2$ from simulations. The $\Delta\chi^2$ values represent the difference between the unreduced χ^2 of the absorbed power law model and the combined blackbody and power law model. The left panel shows the results for the “weak” blackbody component relative to power law for 500 simulated spectra at 400 counts (top) and 2000 counts (bottom). The right panel shows the results for the “strong” blackbody component. For a weak blackbody component at 400 counts, the thermal component is undetectable. However, it is able to be distinguished as the number of counts is increased. A strong blackbody component is easily distinguishable at 400 counts.

A.2. Simple Power Law Model

Our next set of simulations sought to determine our confidence in the simple power law fit being an adequate descriptor of the spectra. Binning provides a problem in distinguishing between a powerlaw and a curvature in the spectrum at the low energy range, since the binning procedure can wash out a low kT blackbody from the spectrum. For this reason, we chose to simulate unbinned PN spectra for a source we categorized as a low-state object, IC 0342 XMM1. IC 0342 XMM1 represents characteristics typical of our low-state candidates, namely it is within the proper luminosity range and it has a power law index of $\Gamma \approx 1.7$ (the median of the distribution for low-state objects is 2.03) and a hydrogen column density near the median of all the fitted values (where the median value is $\approx 3 \times 10^{21} \text{ cm}^{-2}$ and the value of IC 0342 X-1's column density is $5.8 \times 10^{21} \text{ cm}^{-2}$). We chose this source for these reasons and the high number of counts in its PN spectrum. Instead of using the χ^2 statistic (used for binned data), we chose to use the maximum-likelihood statistic, $C\text{-stat}$, in *XSPEC* (which uses unbinned data).

We simulated 500 spectra using the best-fit parameters for the simple power law fit using the *fakeit* command. We fit the simulated spectra with two models: the simple powerlaw and a combined blackbody and power law model and computed the change in the goodness of fit, $\Delta\chi^2$. For the two-component model, once again we placed the constraint that the blackbody temperature remain in the range that it would be detectable by *XMM-Newton*, 0.07 - 4 keV. We followed this procedure for 1000, 2000, and 4000 counts. At both the 1000 and 2000 count level, the addition of a second component has no effect on the C-statistic (the distributions in C-space for both the power law fit and the two-component fit are indistinguishable).

At the 4000 count level, the C-statistic distributions for the two models separate such that there is an 26% confidence that the two-component model is a better fit to the data. We find, when we examine the model parameters, that the power law index (Γ) for the two-component model ranges between 1.19 – 2.12 with the mean value ≈ 1.74 . The mean value for all three count levels used clustered around this value, though the range in Γ increased as the counts decreased. The mean blackbody temperature for simulations with 4000 counts was 1.17 keV (with the range varying between the amount previously noted) with a median of 1.06 keV. For simulations with lower counts, the blackbody temperature becomes higher (1.24 keV for 1000 counts) with a higher median (1.83 keV for 1000 counts). This tells us that the fitting procedure tends to approximate a pure power law spectrum as a two-component spectrum with Γ equal to that of the true spectral index but with a blackbody temperature higher than those observed in our study (1.1 keV or higher) which in the *XMM* band can be approximated as a power law. If we found spectra in our sample that were best fit with a low spectral index and a high blackbody temperature, we might suspect that the spectrum's true nature is a power law. We also note that if the hydrogen column density is large, much $> 3 \times 10^{21} \text{ cm}^{-2}$, a low temperature (kT) blackbody component can be much more difficult to detect.

B. Additional Spectral Fits

The following sources were not best fit by the standard models employed in this study:

B.1. NGC300 XMM4

This source was classified as a super-soft X-ray source by Kong & DiStefano (2003). We find that the standard single-component absorbed blackbody model is a much better model for this spectrum. In fact, the power law, bremsstrahlung, and combined models do not fit the data within the 90% confidence range. Fitting an absorbed blackbody, we find the best fit corresponds to the following parameters: $n_H = 1.38_{-0.55}^{+0.27} \times 10^{21} \text{ cm}^{-2}$, $kT = 0.059_{-0.005}^{+0.007} \text{ keV}$, and $\chi^2/\text{dof} = 74.5/45$. This fit yields an unabsorbed flux of $3.3 \times 10^{-13} \text{ erg cm}^{-2} \text{ s}^{-1}$.

B.2. NGC4631 XMM4

The spectrum of this source clearly identifies it as a super-soft X-ray source. As with NGC300 XMM4, the standard models employed in this study did not adequately match the data. The best fitting model corresponds again to an absorbed blackbody. The corresponding parameters are as follows: $n_H = 6.2_{-1.5}^{+0.26} \times 10^{21} \text{ cm}^{-2}$, $kT = 0.07_{-0.01}^{+0.01} \text{ keV}$, and $\chi^2/\text{dof} = 142.3/74$. This fit yields an unabsorbed flux of $9.5 \times 10^{-12} \text{ erg cm}^{-2} \text{ s}^{-1}$. The position of this source shows it to be coincident with a globular cluster associated with that galaxy. This source was identified as a bulge X-ray source, possibly powered by accretion, in a ROSAT study of NGC4631 (Vogler & Pietsch 1996).

B.3. NGC4631 XMM5

The spectrum of this source was best fit with an absorbed power law + an absorbed *vapec* model. This indicates the presence of hot gas, indicating a possible thermal X-ray source.

B.4. NGC4945 XMM5

The spectrum of this source was not adequately fit with any of the standard models used in this investigation. The spectrum exhibits a prominent Fe K line in the PN spectrum that is well fit by a gaussian (*zgauss*) at 6.4 keV. We find that the entire spectrum is best fit with a partial covering fraction absorption model (*pcfabs*) in combination with the normal absorption, a power law, and a gaussian. The best fit parameters yield: absorption column density, $n_H = 1.79 \times 10^{21} \text{ cm}^{-2}$, partial covering absorption, $n_H = 18.4 \times 10^{21} \text{ cm}^{-2}$, partial covering fraction = 0.82, $\Gamma = 1.6$, and $\chi^2/\text{dof} = 61.8/57$. The source is clearly located within the optical galaxy, and is thus unlikely to

be a background AGN.

B.5. M51 XMM5

The spectrum and luminosity ($L_X \approx 1.9 \times 10^{42} \text{ erg s}^{-1}$) of this source suggests that it is an AGN. The location of the source, from the Digital Sky Survey, places it within the dwarf companion of M51 making a value of the optical flux hard to constrain. The best fit to this source was an absorbed blackbody + power law and the spectral parameters are listed in Table 4.

B.6. M83 XMM2

Like NGC4945 XMM5, this source was best fit by a partial absorption model. However, this source showed no evidence of an Fe K line. We fit this source's spectra using a partial covering fraction absorption model in combination with the normal absorption model and a power law. The best fit parameters yield: absorption column density, $n_H = 2.1 \times 10^{21} \text{ cm}^{-2}$, partial covering absorption, $n_H = 43.5 \times 10^{21} \text{ cm}^{-2}$, partial covering fraction = 0.86, $\Gamma = 2.95$, and $\chi^2/\text{dof} = 83.5/84$. The unabsorbed flux in the range of 0.3-10 keV equals $1.37 \times 10^{-12} \text{ erg cm}^{-2} \text{ s}^{-1}$.

B.7. Inverse Compton Scattering Sources

Table 7 includes the parameters for the “ULX” sources best fit by the *compST* model. A discussion of these sources and interpretation of the data is included in section 5.2.

C. Additional Tables

Table C1. Bright Point Sources Examined

Source ¹	RA (h m s)	Dec (° / ′ / ″)	Total Counts	Count Rate ²	ID	Location in galaxy ³	XMM ref ⁷
NGC247 XMM1	00 47 03.8	-20 47 46.2	3458, 1389, 1379	20.33, 5.8, 6.4	1RXS J004704.8-204743	sa	-
NGC247 XMM2	00 47 03.1	-20 37 02.5	-, 597, 600	-, 1.9, 1.4	-	sa	-
NGC253 XMM1	00 47 32.8	-25 17 52.6	-, 3156, 2985	-, 11.38, 9.9	NGC253 PSX-2 ⁴	near center	1
...	-, 12654, 12812	-, 8.7, 9.1	...	-	
NGC253 XMM2	00 47 22.4	-25 20 55.2	-, 825, 942	-, 2.8, 2.97	NGC253 PSX-5	sa	1
...	-, 10347, 10304	-, 8.2, 8.5	...	-	
NGC253 XMM3	00 47 35.2	-25 15 13.8	-, 870, 1065	-, 3, 3.41	NGC253 PSX-7	sa	1
...	-, 5988, 6131	-, 4.2, 4.6	...	-	
NGC253 XMM4	00 47 23.3	-25 19 06.5	-, 649, 703	-, 1.4, 1.3	-	sa	-
...	-, 3823, 3738	-, 1.7, 1.95	-	-	
NGC253 XMM5	00 47 17.6	-25 18 12.1	-, 295, 313	-, 1.08, 1.04	NGC253 PSX-4	sa	2
...	-, 4199, 4303	-, 3.6, 3.8	...	-	
NGC253 XMM6	00 47 42.8	-25 15 05.5	-, 6081, 6407	-, 3.8, 4.4	NGC 0253 [VP99] X40	sa	1
NGC253 XMM7 ⁵	00 47 09.2	-25 21 21.7	-, 4300, 4454	-, 2.6, 3.0	-	sa	-
NGC300 XMM1	00 55 09.9	-37 42 13.9	6778, 2248, 2453	18.6, 4.9, 5.4	-	sa	-
NGC300 XMM2	00 55 10.6	-37 48 36.7	1364, 456, 463	3.1, 0.9, 0.9	-	edge sa?	-
NGC300 XMM3	00 54 49.7	-37 38 53.8	915, 442, 435	2.2, 0.9, 0.9	-	sa ⁶	-
NGC300 XMM4	00 55 10.9	-37 38 53.8	745, 224, 233	1.9, 0.3, 0.4	XMMU J005511 -3749; SSS	sa	3
NGC300 XMM5	00 55 21.1	-37 29 19.5	750, 247, 250	1.7, 0.4, 0.5	-	out	-
NGC300 XMM6	00 54 44.2	-37 51 04.5	517, 187, 165	1.1, 0.3, 0.3	-	out	-
NGC625 XMM1 ⁸	01 35 06.8	-41 26 17.1	5832, 577, 2119	3, 0.6, 1.4	-	sa	-
NGC1313 XMM1	03 18 19.9	-66 29 10.7	2876, 900, 810	8.6, 3.2, 2.8	NGC1313 [CPS95] X-1; IXO 07	sa	4,5
NGC1313 XMM2	03 17 38.8	-66 33 05.3	7568, 2357, 2108	25.4, 8.8, 7.8	NGC1313 [CPS95] X-3; SN 1978 K	edge sa	6
NGC1313 XMM3	03 18 22.5	-66 36 06.2	6960, 2179, 1793	23.3, 8.1, 6.6	NGC1313 [CPS95] X-2; IXO 08	edge sa?	4,5
NGC1313 XMM4	03 18 18.5	-66 30 05	2075, 659, 567	5.1, 1.8, 1.5	NGC1313 [SPC2000] X-8	near center	-
IC0342 XMM1	03 45 55.8	+68 04 54.5	1802, 1216, 1105	33.6, 12.4, 11.1	IC0342 [RW2000] X-1; IXO 22	sa	5, 7, 8
IC0342 XMM2	03 46 15.0	+68 11 11.2	1147, 541, 184	21.1, 5.5, 1.7	IC0342 [RW2000] X-3	sa	7, 8
IC0342 XMM3	03 46 48.6	+68 05 43.2	1186, 670, 606	21.7, 6.8, 6.0	IC0342 [LLJ2000] X-2	near center	7, 8
IC0342 XMM4	03 46 57.2	+68 06 20.2	551, 338, 377	9.5, 3.9, 3.6	IC0342 [RW2000] X-6	near center	7, 8
NGC1569 ⁹	
NGC1705 XMM1	04 54 57.6	-53 24 23.5	1174, 400, 371	2.4, 0.6, 0.6	RX J0454.9-5324	out?	-
NGC1705 XMM2	04 54 19.6	-53 20 41.9	933, 375, 397	1.9, 0.6, 0.6	...	out?	-
NGC1705 XMM3	04 54 38.1	-53 18 16.2	698, 372, 418	1.4, 0.6, 0.6	WGA J0454.7-5318	out?	-
MRK71 XMM1	07 28 51.8	+69 07 27	832, 225, 207	3.9, 0.97, 0.9	-	out	-
NGC2403 XMM1	07 36 25.6	+65 35 40	-, 1199, 672	-, 1.0, 0.60	NGC2403 [RW2000] X-1	edge sa	-

Table C1—Continued

Source ¹	RA (h m s)	Dec (° ′ ″)	Total Counts	Count Rate ²	ID	Location in galaxy ³	XMM ref ⁷
NGC2403 XMM2	07 36 50.2	+65 36 02.1	1964, 729, 672	1.99, 0.63, 0.60	-	near center	-
NGC2403 XMM3	07 36 55.4	+65 35 40.3	1497, 489, 378	1.4, 0.40, 0.33	-	near center	-
NGC2403 XMM4	07 37 02.5	+65 39 35.2	1004, 274, 288	0.52, 0.15, 0.21	NGC2403 [RW2000] X-4	edge sa?	-
Hol II XMM1	08 19 28.8	+70 42 20.3	31052, 1257, 10807	272.2, 75.5, 72.7	Holm II X-1; IXO 31 ¹⁰	near center?	9
...	3853, 1361, 1452	78.3, 18.9, 20.5	...	-	-
Hol I XMM1	09 41 30	+71 12 34	687, 768, 754	2.9, 2.7, 2.6	-	out?	-
Hol I XMM2	09 39 59.7	+71 06 40.2	575, 203, 224	2.5, 0.7, 0.7	1WGA J0940.0+7106	out?	-
Hol I XMM3	09 42 06.7	+71 04 45.3	452, 141, 141	1.7, 0.4, 0.4	-	out?	-
M81 XMM1	09 55 32.9	+69 00 34.8	50788, -, 18988	51.1, -, 21.7	NGC3031 [RW2000] X-11	sa	-
...	-, 1227, - ¹¹	-, 12, 13.1	...	-	-
M81 XMM2	09 55 24.8	+69 01 11.7	17871, -, 4121	13.2, -, 4.4	SN 1993J	sa	10
M81 XMM3	09 55 10.6	+69 05 02.2	-, -, 1970	-, -, 1.5	NGC3031 [RW2000] X-05	sa	-
M81 XMM4	09 55 24.3	+69 10 00.2	-, -, 1197	-, -, 1.0	NGC3031 [RW2000] X-08	edge sa	-
M81 XMM5	09 55 49.2	+69 05 30.5	-, -, 2077	-, -, 2.3	-	sa	-
M82 ¹²	-
Hol IX XMM1	09 57 53.3	+69 03 48.7	14976, 6546, 6586	207.3, 64.3, 65	Hol IX X-1; IXO 34	?	4, 5
Sextans A XMM1	10 11 24.6	-04 42 17.2	3963, 1323, 1242	17.2, 5, 4.5	-	out	-
IC2574 XMM1	10 28 42.4	+68 28 17.8	1047, 673, 623	8.3, 2.6, 2.5	-	sa	-
IC2574 XMM2	10 26 33.5	+68 29 32.1	533, 335, 300	4.3, 1.3, 1.2	-	out	-
IC2574 XMM3	10 27 22.2	+68 18 47.6	538, 293, 301	4.2, 1.1, 1.2	-	out	-
NGC4214 XMM1	12 15 37.0	+36 19 29.4	434, 230, 225	2.9, 1.6, 1.5	NGC4214 [HSS2004] 11	sa	-
NGC4214 XMM2	12 15 58.2	+36 22 38.5	626, 160, 285	3.4, 0.6, 1.5	-	out	-
NGC4258 XMM1 ⁵	12 18 47.8	+47 20 51.7	828, 470, 444	7.0, 2.8, 2.8	-	sa	-
...	-	-
NGC4258 XMM2	12 18 57.8	+47 16 06.8	732, 337, 337	5.8, 2, 2.1	NGC4258 [RW2000] X-7	sa	-
...	716, 268, 290	1.8, 1, 1.0	...	-	-
NGC4258 XMM3	12 18 56.5	+47 21 24.3	489, 182, 184	3.8, 0.9, 1.1	NGC4258 [RW2000] X-5	sa	-
...	-, 160, 142	-, 0.3, 0.3	...	-	-
NGC4258 XMM4	12 19 23.2	+47 09 37.2	644, 277, 224	4.9, 1.3, 1.3	HELLAS 288	edge sa?	-
...	964, 410, 382	0.3, 0.2, 0.1	...	-	-
NGC4395 XMM1	12 26 01.5	+33 31 29	2162, 862, 921	15.5, 5.1, 5.6	NGC4395 [RW2000] X-1; IXO 53	sa	-
NGC4395 XMM2	12 25 25.3	+33 36 46.4	392, 252, 208	2.6, 1.5, 1.2	-	sa?	-
NGC4395 XMM3	12 25 32.6	+33 25 27.9	763, 277, 278	5.2, 1.5, 1.6	-	out?	-
NGC4395 XMM4	12 25 42.7	+33 40 00.1	516, 60, 40	3.1, 0.3, 0.2	-	out	-
NGC4449 XMM1	12 28 18	+44 06 30.9	1409, 608, 593	10.6, 3.6, 3.5	XRB?; NGC4449 [RW2000] X-7; Source 27 ¹³	sa	-

Table C1—Continued

Source ¹	RA (h m s)	Dec (° / ′ / ″)	Total Counts	Count Rate ²	ID	Location in galaxy ³	XMM ref ⁷
NGC4449 XMM2	12 28 09.3	+44 05 03.9	1503, 527, 586	11.3, 3.1, 3.5	SNR?; NGC4449 [RW2000] X-1; Source 10	sa	-
NGC4449 XMM3	12 28 11.1	+44 06 43.9	1094, 549, 404	8.3, 3.2, 2.3	SNR; Source 15	sa	-
NGC4490 XMM1	12 30 32.4	+41 39 14.6	746, 323, 393	6.0, 1.9, 2.2	NGC4490 [RW2000] X-1	sa	-
NGC4490 XMM2	12 30 36.5	+41 38 33.3	656, 299, 310	5.3, 1.7, 1.7	NGC4490 [RW2000] X-2	near center	-
NGC4490 XMM3	12 30 43.3	+41 38 11.5	832, 501, 461	5.8, 2.6, 2.2	NGC4490 [RW2000] X-4	sa	-
NGC4490 XMM4	12 30 31.1	+41 39 08.1	546, 291, 286	4.4, 1.7, 1.6	CXOU J123030.8 +413911	sa	-
NGC4490 XMM5	12 30 30.3	+41 41 40.3	413, 587, 482	2.7, 3.1, 2.3	NGC4485 [RW2000] X-1	sa	-
NGC4631 XMM1	12 41 55.8	+32 32 14	5093, 1969, 1762	13, 4.2, 3.8	NGC4631 [RW2000] X-1; IXO 68	sa	-
NGC4631 XMM2	12 41 57.5	+32 32 01	1273, 531, 400	3.3, 1.2, 0.9	NGC4631 [RW2000] X-2	sa	-
NGC4631 XMM3	12 41 58.2	+32 28 49.6	1271, 443, 457	2.8, 0.9, 0.9	CXOUSEXSI J124158.0+322851	out	-
NGC4631 XMM4	12 42 16.1	+32 32 48.8	957, 400, 429	2.3, 0.8, 0.8	[VP96] H13	sa	-
NGC4631 XMM5	12 42 11.2	+32 32 33.6	1626, 894, 866	3.9, 1.9, 1.8	[VP96] H12; [HFE2003] PSX-01	sa	-
NGC4736 XMM1	12 50 50.2	+41 07 12	713, 273, 227	6.7, 2.1, 1.7	NGC4736 X-4 ¹⁴	near center	-
NGC4945 XMM1	13 05 33.3	-49 27 36.3	1456, 646, 595	7.9, 2.9, 2.6	NGC4945 [GMB2000] X-2	sa	-
NGC4945 XMM2	13 05 38.4	-49 25 45.3	1393, 600, 523	7.6, 2.7, 2.3	NGC4945 [R97] X-3	sa	-
NGC4945 XMM3	13 05 18.8	-49 28 24	-, 357, 362	-, 1.6, 1.6	...	sa	-
NGC4945 XMM4	13 05 22.2	-49 28 26.3	731, 331, 332	4.0, 1.5, 1.5	NGC4945 [BIR96] X-1?	sa	-
NGC4945 XMM5	13 05 25.7	-49 28 30.7	772, 267, 301	4.2, 1.2, 1.32	...	sa	-
NGC5204 XMM1	13 29 38.5	+58 25 03.6	9981, 3352, 3384	62.8, 17.7, 17.9	NGC5204 [RW2000] X-1; IXO 77	sa	11
...	9231, 2284, 2349	85.5, 24.7, 25.8	...	-	
NGC5204 XMM2	13 29 27.4	+58 25 31.8	573, 170, 231	3.4, 0.8, 1.2	-	edge sa	-
...	772, 161, 121	5.0, 1.7, 1.1	...	-	
M51 XMM1	13 29 40	+47 12 36.2	1102, 367, 409	6.2, 1.8, 2	NGC5194 [RW2000] X-1	sa	-
M51 XMM2	13 30 07.7	+47 11 04.8	514, 540, 549	2.6, 2.2, 2.2	IXO 81	sa	-
M51 XMM3	13 30 01.1	+47 13 41.4	1004, 315, 311	4.1, 1.1, 1.1	CXOU J133001.0 +471344; IXO 80	sa	-
M51 XMM4	13 30 06	+47 15 38.9	518, 183, 166	2.8, 0.9, 0.8	NGC 5195 [RW2000] X-1	sa	-
M51 XMM5	13 29 59.6	+47 15 54	1079, 359, 257	5, 1.5, 1	CXOU J132959.5 +471559	near center	-
M51 XMM6	13 29 57.5	+47 10 45.3	536, 206, 247	1.9, 0.6, 0.8	CXOU J132957.6 +471048	sa	-
M51 XMM7	13 29 53.6	+47 14 31.5	452, 141, 143	2.4, 0.6, 0.7	CXOU J132953.8 +471432	edge sa	-
M83 XMM1	13 37 19.8	-29 53 49.8	3074, 927, 987	12, 3.3, 2.5	RX J133719 -2953.6; IXO 82	sa	-
M83 XMM2	13 36 59.4	-29 49 57.2	1133, 371, 397	4, 1.3, 1	CXOU J133659.4 -294959	sa	-
M83 XMM3 ¹⁵	13 37 04.4	-29 51 24	1724, 576, 459	7.2, 2.3, 1.2	CXOU J133704.3 -295121	sa	-
M83 XMM4	13 37 01.5	-29 53 26	1289, 345, 401	4.9, 1.3, 1.0	CXOU J133701.4 -295326	sa	-
NGC5253 ¹⁶
M101 XMM1	14 03 14.7	+54 18 05	2690, 1449, 1417	10.3, 3.3, 3.3	CXOU J140313.9 +541811; XMM-2 ¹⁷	sa	12

Table C1—Continued

Source ¹	RA (h m s)	Dec (° / ′ / ″)	Total Counts	Count Rate ²	ID	Location in galaxy ³	XMM ref ⁷
M101 XMM2	14 03 03.8	+54 27 37	2825, 1623, 1551	10.3, 3.6, 3.3	XMM-1	edge sa?	12
M101 XMM3	14 04 14.6	+54 26 04.4	1460, 822, 717	5, 1.6, 1.3	CXOU J140414.3 +542604; XMM-3	edge sa?	12
M101 XMM4	14 02 28.5	+54 16 26.7	1505, 877, 757	5.1, 1.7, 1.5	CXOU J140228.3 +541626	sa	12
M101 XMM5	14 02 22.5	+54 17 58	516, 245, 289	1.8, 0.4, 0.6	CXOU J140222.2 +541756; XMM-6	sa	12
NGC5408 XMM1	14 03 19.8	-41 22 59.3	5932, 2036, 2077	12.8, 3.2, 3.3	NGC5408 [KCP2003] X-1	sa	5
CIRCINUS XMM1 ¹⁸	14 12 54.2	-65 22 55.3	16220, 11452, -	14.5, 11.3, -	-	edge sa?	-
CIRCINUS XMM2	14 12 39.2	-65 23 34.3	8741, 2386, -	5.7, 1.9, -	-	edge sa?	-
CIRCINUS XMM3	14 13 28.3	-65 18 08.3	4873, 1031, -	1.8, 0.7, -	-	edge sa?	-

¹Sources labeled *XMM-n* in order of apparent brightness from the first observation studied

²count rate units of $\times 10^{-2}$ cts s⁻¹ for the PN, MOS1, and MOS2 spectra

³ocation specified as: inside the optical extent of the galaxy or in spiral arms (sa), near the center of the galaxy, at the edge of a spiral arm/ optical extent of galaxy, or outside the optical extent of the galaxy. Location based on DSS images.

⁴identification for NGC0253 following Humphrey et al. (2003)

⁵Transient.

⁶Appears as an extended source in HST image.

⁷references to studies using *XMM-Newton* spectra

⁸Spectra too scattered to model.

⁹bright sources coincide with nucleus (unresolvable star cluster and X-ray binaries), fore-ground star, and background AGN (Martin, Kobulnicky, Heckman (2002)

¹⁰IXO designation from Colbert & Ptak (2002)

¹¹Spectrum from Hol IX observation.

¹²bright source is too close to other sources

¹³Chandra observations of point sources in NGC4449 published in Summers et al. (2003); Source 27 varied from ROSAT observations

¹⁴three other sources near the nucleus are unresolvable in the XMM obs., but seen by Chandra (Eracleous et al. 2002)

¹⁵Unable to model spectrum due to an error in χ^2 -space

¹⁶bright sources are too close, but resolvable by Chandra (Summers et al. 2004)

¹⁷alternate ID from Jenkins et al. (2004)

¹⁸bright sources near the nucleus are unresolvable, but seen by Chandra (Smith & Wilson 2001)

References. — (1) Pietsch et al. 2001; (2) Pietsch, Haberl, & Vogler 2003; (3) Kong & Di Stefano 2003; (4) Miller et al. 2004; (5) Wang et al. 2004; (6) Schlegel et al. 2004; (7) Bauer, Brandt, & Lehmer 2003; (8) Kong 2003; (9) Lehmann et al. 2005; (10) Zimmermann & Aschenbach 2003; (11) Roberts et al. 2005; (12) Jenkins et al. 2004.

Table C2. Bright, Identifiable Background and Foreground Sources

Galaxy	RA (h m s)	Dec ($^{\circ}$ / $''$)	Identification
NGC 247	0 46 51.7	-20 43 30	QSO B044-2059
NGC 300	0 55 26.7	-37 31 25.6	HD 5403 (Star)
NGC 625	01 34 42.4	-41 36 15.2	QSO B0132-4151
NGC 1569 ^a	04 31 16.9	+64 49 50	CXOU J043116.8+644950 (Star)
NGC 1569	04 31 14.2	+64 51 07.9	CXOU 043114.0+645107 (Star)
NGC 1569	04 31 25.4	+64 51 53.8	CXOU 043125.1+645154 (AGN)
NGC 1705	04 54 01.2	-53 21 12.3	WGA J0454.0-5320 (M star or elliptical galaxy)
NGC 2403	07 35 09	+65 40 27.5	HD 59581 (Star)
NGC 4258	12 18 08.9	+47 16 08.3	QSO J1218+472
M83	13 36 45.6	-29 59 13.9	2MASX J13364579-2959122 (Galaxy)
M83	13 36 13.9	-29 56 13	RX J133615-2957.8 (Galaxy)
NGC 5253	13 39 50.6	-31 34 11.1	CD-30 10790 (Star)
M101	14 02 30	+54 21 18.2	[WIP99] H13 (Star) ^b
NGC 5408	14 03 27.5	-41 25 18.5	(Star)

^aidentification for objects in NGC 1569 from Martin, Kobulnicky, & Heckman (2002)

^bconfirmed by K. Kuntz using HST ACS

Table C3. *XMM-Newton* power law fit for best fit two-component spectra

Source	n_H^a	Γ	χ^2/dof	F_X^c	L_X^d
NGC247 XMM1	$9.5^{+1.6}_{-1.4}$	$8.52^{+1.14}_{-0.91}$	112.2/95	1900	2200
NGC253 XMM1	$3.4^{+0.3}_{-0.3}$	$1.77^{+0.06}_{-0.06}$	262.6/232	3.1	3.6
...	$6.9^{+0.4}_{-0.4}$	$1.98^{+0.05}_{-0.05}$	611.6/582	2.9	3.3
NGC253 XMM2 (obs 2)	$2.2^{+0.1}_{-0.1}$	$2.03^{+0.04}_{-0.04}$	507.4/500	1.2	1.4
NGC253 XMM3	$3.9^{+0.5}_{-0.4}$	$2.17^{+0.14}_{-0.11}$	91.9/83	0.73	1.2
...	$4.0^{+0.4}_{-0.3}$	$2.06^{+0.09}_{-0.07}$	381.8/409	0.98	1.6
NGC253 XMM4	$8.5^{+3.0}_{-2.3}$	$2.09^{+0.33}_{-0.28}$	73.6/59	0.52	0.85
...	$1.2^{+0.3}_{-0.3}$	$2.09^{+0.16}_{-0.15}$	321.4/293	0.29	0.48
NGC253 XMM5	$1.7^{+1.2}_{-0.9}$	$1.54^{+0.22}_{-0.20}$	31.8/25	0.32	0.53
...	$3.4^{+0.2}_{-0.2}$	$2.17^{+0.7}_{-0.7}$	283.8/298	1.1	1.3
NGC253 XMM6	$3.9^{+0.3}_{-0.3}$	$2.21^{+0.84}_{-0.80}$	435/409	0.93	1.5
NGC253 XMM7	$7.1^{+0.7}_{-0.7}$	$2.15^{+0.11}_{-0.11}$	357/342	1.3	2.2
NGC300 XMM1	$0.97^{+0.11}_{-0.11}$	$2.67^{+0.06}_{-0.06}$	469.8/422	0.81	0.6
NGC300 XMM2	$1.7^{+0.40}_{-0.40}$	$3.20^{+0.32}_{-0.24}$	133.98/99	0.27	0.21
NGC300 XMM3	$3.4^{+0.8}_{-0.6}$	$1.86^{+0.15}_{-0.13}$	101.9/81	0.19	0.15
NGC300 XMM5	0.311 ^e	$2.29^{+0.18}_{-0.14}$	54.2/56	0.14	0.10
NGC300 XMM6	? ⁺	$2.05^{+0.17}_{-0.15}$	47.6/37	0.06	0.15
NGC1313 XMM1	$1.5^{+0.2}_{-0.2}$	$1.81^{+0.08}_{-0.09}$	219.8/203	0.42	0.88
NGC1313 XMM2	$2.8^{+0.16}_{-0.16}$	$2.48^{+0.07}_{-0.06}$	464.1/421	1.9	4.0
NGC1313 XMM3	$3.6^{+0.2}_{-0.2}$	$3.2^{+0.09}_{-0.09}$	778.3/426	3.3	6.9
IC0342 XMM3	$3.8^{+0.4}_{-0.4}$	$2.58^{+0.15}_{-0.14}$	185.8/109	1.7	3.1
NGC1705 XMM1	0.3 ^e	$1.93^{+0.11}_{-0.10}$	61.9/88	0.12	0.37
NGC1705 XMM2	$1.4^{+0.45}_{-0.41}$	$2.12^{+0.26}_{-0.25}$	91/76	0.078	0.24
NGC1705 XMM3	$0.6^{+0.36}_{-0.40}$	$1.36^{+0.12}_{-0.13}$	80.9/67	0.17	0.53
NGC2403 XMM1	$3.2^{+0.61}_{-0.55}$	$2.15^{+0.16}_{-0.15}$	92.2/81	2.2	3.6
NGC2403 XMM2	$2.7^{+0.37}_{-0.34}$	$2.07^{+0.11}_{-0.11}$	179.5/151	1.3	2.0
NGC2403 XMM3	$1.9^{+0.40}_{-0.36}$	$1.97^{+0.14}_{-0.13}$	92.6/107	0.81	1.3
HolmII XMM1 (obs 1)	$1.5^{+0.07}_{-0.07}$	$2.61^{+0.04}_{-0.04}$	1134.2/976	12	10
Holm I XMM1	? ⁺	$2.04^{+0.14}_{-0.07}$	102.8/95	0.48	1.7
M81 XMM1	$3.2^{+0.07}_{-0.07}$	$2.09^{+0.02}_{-0.02}$	1849.9/1245	4.5	7.0
...	$3.0^{+0.3}_{-0.3}$	$1.79^{+0.07}_{-0.07}$	224.9/208	4.3	6.7
M81 XMM2	7.3	6.13	1358.2/618	48.5	75.2
M81 XMM3	$0.97^{+0.25}_{-0.41}$	$1.58^{+0.18}_{-0.15}$	81.35/80	2.5	3.9
M81 XMM4	? ⁺	$0.88^{+0.11}_{-0.11}$	66.4/52	0.35	0.54
M81 XMM5	$1.0^{+0.4}_{-0.3}$	$1.52^{+0.11}_{-0.11}$	97.5/82	0.44	0.68
Holm IX XMM1	$1.7^{+0.08}_{-0.08}$	$1.84^{+0.03}_{-0.03}$	1000.9/882	9.4	15
Sextans A XMM1	$0.18^{+0.23}_{-0.16}$	$2.25^{+0.12}_{-0.07}$	271.4/275	0.56	0.13
NGC4214 XMM2	$0.2^{+0.5}_{-0.2}$	$2.03^{+0.43}_{-0.28}$	50.9/46	0.16	0.14
NGC4258 XMM1	$1.6^{+0.4}_{-0.4}$	$1.9^{+0.14}_{-0.13}$	101.4/78	0.06	0.04
NGC4258 XMM2 (obs 1)	$3.5^{+0.9}_{-0.7}$	$1.88^{+0.16}_{-0.15}$	97.5/63	0.43	2.6
NGC4395 XMM1	$3.7^{+0.5}_{-0.4}$	$4.93^{+0.34}_{-0.30}$	195.1/156	7.2	14
NGC4395 XMM3	? ⁺	$1.86^{+0.14}_{-0.09}$	55.9/58	0.25	0.48
NGC4449 XMM1	$6.3^{+0.9}_{-0.7}$	$2.22^{+0.14}_{-0.12}$	103/118	1.2	1.36
NGC4449 XMM3	$3.3^{+0.5}_{-0.4}$	$3.36^{+0.29}_{-0.23}$	154/89	1.3	1.5
NGC4490 XMM1	$0.83^{+0.14}_{-0.12}$	$2.53^{+0.17}_{-0.16}$	101.5/65	1.2	8.7
NGC4490 XMM2	$6.3^{+1.3}_{-1.0}$	$2.36^{+0.19}_{-0.17}$	49.5/56	0.92	6.7

Table C3—Continued

Source	n_H^a	Γ	χ^2/dof	F_X^c	L_X^d
NGC4490 XMM3	$9.4^{+1.5}_{-1.2}$	$2.95^{+0.24}_{-0.20}$	76.7/80	1.5	11
NGC4631 XMM1	$2.3^{+0.16}_{-0.15}$	$2.13^{+0.06}_{-0.05}$	383.4/347	0.76	5.1
NGC4631 XMM2	$1.9^{+0.4}_{-0.3}$	$2.01^{+0.14}_{-0.12}$	119.5/99	0.23	1.5
NGC4631 XMM3	$0.63^{+0.3}_{-0.2}$	$1.53^{+0.1}_{-0.08}$	146/98	0.15	1.0
NGC4736 XMM1	$0.95^{+0.6}_{-0.5}$	$2.02^{+0.26}_{-0.25}$	62.8/53	0.36	0.80
NGC4945 XMM1	$5.8^{+0.8}_{-0.7}$	$1.88^{+0.08}_{-0.10}$	116/122	0.9	1.0
NGC4945 XMM2	$3.4^{+0.6}_{-0.5}$	$1.58^{+0.09}_{-0.10}$	114.5/115	0.71	0.82
NGC4945 XMM4	$5.2^{+0.8}_{-0.7}$	$2.59^{+0.19}_{-0.17}$	75.5/62	0.49	0.56
NGC5204 XMM1	$0.61^{+0.1}_{-0.1}$	$2.11^{+0.04}_{-0.04}$	592.1/561	2.0	5.5
...	$1.1^{+0.1}_{-0.1}$	$2.41^{+0.07}_{-0.07}$	533/498	3.0	8.3
M51 XMM1	$1.1^{+0.30}_{-0.27}$	$2.67^{+0.20}_{-0.16}$	110.5/82	0.34	2.8
M51 XMM2	$2.3^{+0.50}_{-0.30}$	$2.50^{+0.22}_{-0.20}$	75.2/70	0.52	3.3
M51 XMM5	2.7	3.08	256.0/72	0.43	2.7
M51 XMM6	$2.0^{+0.83}_{-0.72}$	$2.50^{+0.33}_{-0.25}$	40.97/43	0.13	0.83
M51 XMM7	$0.5^{+0.39}_{-0.46}$	$1.95^{+0.23}_{-0.18}$	37.8/31	0.11	0.66
M83 XMM1	$1.9^{+0.34}_{-0.31}$	$2.32^{+0.13}_{-0.12}$	210.9/211	0.64	2.8
M83 XMM4	$6.0^{+1.8}_{-1.3}$	$2.54^{+0.26}_{-0.23}$	91.4/91	0.4	1.8
M101 XMM1	$0.56^{+0.15}_{-0.14}$	$1.98^{+0.06}_{-0.08}$	303/233	0.45	2.9
M101 XMM2	$2.2^{+0.25}_{-0.23}$	$1.85^{+0.07}_{-0.07}$	288.8/263	0.81	5.3
M101 XMM3	$1.5^{+0.4}_{-0.3}$	$2.70^{+0.21}_{-0.17}$	148.9/133	0.51	3.4
M101 XMM4	$2.2^{+0.45}_{-0.42}$	$2.25^{+0.20}_{-0.17}$	165.7/140	0.38	2.5
M101 XMM5	$1.3^{+0.2}_{-0.3}$	$2.28^{+0.12}_{-0.11}$	47.9/46	0.12	0.8
NGC5408 XMM1	$1.6^{+0.2}_{-0.1}$	$3.57^{+0.12}_{-0.11}$	396.8/339	7.04	19.4
CIRCINUS XMM1	$7.6^{+0.3}_{-0.3}$	$2.15^{+0.05}_{-0.04}$	762.9/863	4.6	8.8
CIRCINUS XMM2	$11.7^{+0.4}_{-0.7}$	$3.48^{+0.13}_{-0.06}$	517.9/432	2.7	5.2
CIRCINUS XMM3	$9.0^{+2.1}_{-1.0}$	$2.57^{+0.40}_{-0.17}$	285.2/262	0.32	0.61

^atotal column density in units of 10^{21} cm^{-2}

^bimprovement in χ^2 over the single-component power law model

^cunabsorbed flux in the 0.3-10 keV band in units of $10^{-12} \text{ erg cm}^{-2} \text{ s}^{-1}$

^dunabsorbed luminosity in the 0.3-10 keV band, using the distances quoted in Table 1, in units of $10^{39} \text{ erg s}^{-1}$

^eabsorption level frozen at Galactic level

Table C4. Best-Fit Absorbed Comptonization Model Parameters

ID	nH ^a	kT ^b	tau ^c	χ^2	F_X ^d
NGC 253 XMM2	$1.8^{+0.08}_{-0.16}$	$1.28^{+0.13}_{-0.12}$	$19.59^{+2.0}_{-1.6}$	464/498	1.47
NGC 2403 XMM1	$1.95^{+1.2}_{-0.6}$	$0.98^{+0.16}_{-0.15}$	$25.4^{+7.2}_{-8.3}$	82.8/85	1.4
NGC 4490 XMM1	$4.7^{+1.1}_{-2.1}$	$0.96^{+0.13}_{-0.16}$	$27.0^{+18.3}_{-4.9}$	66.5/64	0.66
NGC 4490 XMM2	$5.0^{+1.6}_{-1.4}$	$1.21^{+0.21}_{-0.31}$	$18.8^{+8.6}_{-9.7}$	45.7/55	0.67
M101 XMM2	$1.6^{+0.26}_{-0.24}$	$1.24^{+0.09}_{-0.15}$	$23.3^{+3.4}_{-2.8}$	256/262	0.65
M101 XMM3	$1.1^{+0.43}_{-0.40}$	1.13	15.2	128/132	0.41
Circinus XMM2	$6.8^{+1.3}_{-0.9}$	$0.62^{+0.08}_{-0.04}$	$29.7^{+8.1}_{-7.0}$	437.2/430	0.5
Circinus XMM3	$6.7^{+0.6}_{-2.4}$	$0.93^{+0.28}_{-0.24}$	$23.1^{+17.5}_{-5.2}$	273.1/261	0.17

^atotal column density in units of 10^{21} cm $^{-2}$

^btemperature in keV

^coptical depth

^dunabsorbed flux in the 0.3-10 keV band in units of 10^{-12} erg cm $^{-2}$ s $^{-1}$

Table C5. *XMM-Newton* Galaxy Observations

Galaxy	S ₆₀ (Jy)	S ₁₀₀ (Jy)	F _{FIR} ^a	L _{FIR} ^b	No. of ULX
NGC247	7.93	27.32	0.602	0.687	1
NGC253	998.73	1861.67	55.92	93.10	3
NGC300	23.08	74.45	1.688	1.324	0
NGC625	5.09	9.08	0.280	0.230	0
NGC1313	35.97	92.00	2.329	4.845	2
IC0342	255.96	661.68	16.66	30.32	3
NGC1569	45.41	47.29	2.072	0.635	0
NGC1705	0.970	2.580	0.064	0.199	0
MRK 71	3.51	4.67	0.173	0.239	1
NGC2403	51.55	148.49	3.547	5.378	2
Holmberg II	1.15	2.62	0.070	0.061	1
Holmberg I	1
M81	44.73	174.02	3.647	5.655	1
M82	1271.32	1351.09	58.35	106.2	1
Holmberg IX	1
Sextans A	0.255	0.674	0.017	0.004	0
IC 2574	2.41	10.62	0.212	0.329	0
NGC 4214	17.87	29.04	0.947	0.826	1
NGC 4258	21.60	78.39	1.690	10.48	1
NGC4395	4.21	12.90	0.299	0.573	1
NGC4449	37.00	58.28	1.937	2.199	1
NGC4490	47.79	85.94	2.636	19.19	5
NGC4631	82.90	208.66	5.324	35.83	1
NGC4736	62.41	135.34	3.734	8.261	4
NGC4945	588.11	1415.5	36.95	42.49	0
NGC 5204	2.33	5.35	0.143	0.395	2
M51	108.68	292.08	7.213	44.74	5
M83	266.03	638.63	16.69	76.79	0
NGC5253	30.00	30.92	1.365	16.72	0
M101	88.04	252.84	6.048	39.63	4
NGC5408	2.825	2.958	0.129	0.356	1
Circinus	248.7	315.85	12.06	23.10	4

^aflux in units of 10^{-9} erg cm $^{-2}$ s $^{-1}$

^bfar-infrared luminosity in units of 10^{42} erg s $^{-1}$